Idealized Large-Eddy Simulations of a Tropical Cyclone–like Boundary Layer

BENJAMIN W. GREEN AND FUQING ZHANG

Department of Meteorology, The Pennsylvania State University, University Park, Pennsylvania

(Manuscript received 26 August 2014, in final form 12 January 2015)

ABSTRACT

The tropical cyclone (TC) boundary layer (TCBL)—featuring extreme winds over a rough ocean—is difficult to study observationally. With increasing computational power, high-resolution large-eddy simulation (LES) has become an attractive tool to advance understanding of the TCBL. Here, an idealized Cartesian-based LES is employed to investigate boundary layers driven by extreme TC-like winds. The LES includes the effects of centripetal acceleration through an "effective" Coriolis parameter $f^* = f + 2V_g/R$, with the Earth Coriolis parameter f, gradient wind V_g, and (fixed) radius R. Multiple LES experiments are conducted to elucidate how the boundary layer develops and persists in the strongly rotating TC environment. In all simulations, an overshooting jet develops, the height of which increases with V_g, R, and surface drag. Normalized jet strength also increases with R and drag but decreases with V_g. Turbulent diffusivity K_m—which must be parameterized in mesoscale and global models but can be diagnosed by LES—varies considerably both within and among simulations. Also evident is a pseudo-inertial oscillation with a period close to the theoretical $2\pi/f^*$ and an amplitude that decreases exponentially with time. The LES simulations agree with the linear theory for partial-slip Ekman spirals, except when the effects of K_m overwhelmingly counter the effects of V_g.

1. Introduction

The boundary layer is arguably the most important part of a tropical cyclone (TC). For one, the boundary layer is intricately linked to nearly all of the TC-associated threats to life and property: storm surge, violent straight-line winds, and tornadoes. Additionally, the boundary layer plays a critical role in TC development, structure, maintenance, and decay (e.g., Bryan and Rotunno 2009; Smith et al. 2009; Bao et al. 2012; Bryan 2012; Rotunno and Bryan 2012; Gopalakrishnan et al. 2013). The problem is that the boundary layer is also one of the least understood aspects of a TC: incredible shear-driven atmospheric turbulence atop an ocean surface with significant swell and breaking waves makes direct measurement of boundary layer fluxes and other relevant statistics difficult (Black et al. 2007; French et al. 2007; Zhang et al. 2008a,b).

Numerical simulations of any atmospheric boundary layer continue to be constrained by the amount of computational power available. With limited exceptions (e.g., Zhu 2008; Rotunno et al. 2009), few TC simulations have explicitly resolved boundary layer turbulence; its effects on the mean flow are otherwise determined by boundary layer parameterization schemes. The simplest parameterizations use flux-gradient theory: a first-order turbulence closure that relates turbulent fluxes to gradients of mean quantities. For example, given zonal velocity $u = \overline{u} + u'$, meridional velocity $v = \overline{v} + v'$, and vertical velocity $w = \overline{w} + w'$ (overbars and primes denote means and perturbations, respectively), the magnitude of the vertical momentum flux can be related to the magnitude of the mean vertical wind shear by

$$\sqrt{(\overline{u'w'})^2 + (\overline{v'w'})^2} = -K_m \sqrt{\left(\frac{\partial \overline{u}}{\partial z}\right)^2 + \left(\frac{\partial \overline{v}}{\partial z}\right)^2}, \quad (1)$$

where K_m is the vertical component of the eddy diffusivity coefficient for momentum. The problem is that K_m is a strong function of the turbulence. Nevertheless, linear models of the boundary layer (e.g., Eliassen and Lystad 1977; Kepert 2001, hereafter K01) are forced to treat K_m as a global constant; the earliest numerical models of TCs (Ooyama 1969; Rosenthal 1971) assign

Corresponding author address: Mr. Benjamin W. Green, Dept. of Meteorology, The Pennsylvania State University, 503 Walker Bldg., University Park, PA 16802.
E-mail: bwg5019@psu.edu

DOI: 10.1175/JAS-D-14-0244.1

predetermined height-specific values of K_m. A more advanced approach to parameterize boundary layer turbulence in mesoscale models uses the mixing-length hypothesis (e.g., Hong et al. 2006; Bryan and Rotunno 2009; Rotunno and Bryan 2012):

$$K_m = \ell^2 (2\overline{S}_{ij}\overline{S}_{ij})^{1/2} \quad \text{and} \tag{2a}$$

$$\overline{S}_{ij} = \frac{1}{2}\left(\frac{\partial \overline{v}_i}{\partial x_j} + \frac{\partial \overline{v}_j}{\partial x_i}\right), \tag{2b}$$

where ℓ is the mixing length (the size of the large, energy-containing eddies) and $\overline{v}$ is the resolved wind. Mesoscale models—which parameterize all turbulence—usually break up the mixing length into horizontal and vertical components,[1] both of which are often set as global parameters (e.g., Bryan and Rotunno 2009). For the remainder of this manuscript, K_m is only meant to refer to the vertical component of the eddy diffusivity; we do not consider the horizontal eddy diffusivity because (i) large rolls likely make the turbulence anisotropic and (ii) our simulations have no mean gradients in horizontal wind. Even more complex turbulence parameterizations include a nonlocal "countergradient" mixing term to account for transport by the largest eddies in the opposite direction of local gradients (Hong et al. 2006 and references therein). Turbulence parameterization for mesoscale models is by no means straightforward, and various approaches have substantial impacts on the TC boundary layer (Kepert 2010, 2012).

With continually increasing computational capability, numerical simulations that can explicitly resolve the large-scale, energy-containing eddies—so-called large-eddy simulations (LESs; e.g., Moeng 1984; Sullivan et al. 1994; Sullivan and Patton 2011)—are becoming a viable alternative to atmospheric mesoscale models, first for idealized studies and eventually for future operational forecasts. A major benefit of LES is that only the small-scale, non-energy-containing, mainly isotropic turbulent eddies are parameterized [the subgrid-scale component of K_m is calculated based on a form of (2) with ℓ proportional to model grid spacing; see Sullivan et al. (1994)]: no countergradient correction term is needed, and the resolved component of K_m is simply diagnosed from (1). Only a handful of LES studies have considered the atmospheric boundary layer in a TC: those mentioned above (e.g., Zhu 2008; Rotunno et al. 2009) and an analysis of the turbulent structures in a highly idealized, periodic LES (Nakanishi and Niino 2012, hereafter NN12). Also, while not an LES study, Gao and Ginis (2014) explicitly resolved two-dimensional TC boundary layer rolls that were in their linear growth phase. The extensive research on the sensitivity of simulated TCs to surface and other subgrid-scale parameterizations in mesoscale models (e.g., Emanuel 1986, 1995; Braun and Tao 2000; Nolan et al. 2009a,b; Bao et al. 2002, 2012; Green and Zhang 2013, hereafter GZ13, 2014) will no doubt continue with LES. With this in mind, the present study uses an idealized LES to understand the characteristics of a TC-like boundary layer in comparison with existing theories (K01) and modeling studies (particularly NN12).

The remainder of the paper is organized as follows. Section 2 provides an overview of the relevant linear model for TC boundary layers. Section 3 describes the setup of the LES and shows the results of a control simulation. Section 4 deals with the sensitivity experiments. A general discussion can be found in section 5, followed by concluding remarks in section 6.

2. Review of the linear theory of the TC boundary layer

a. *The general case (K01)*

A derivation and analysis of a linear boundary layer model applicable to TCs is presented in K01, which in short linearizes the Ekman layer equations (with a surface slip condition) in cylindrical polar coordinates for a free atmosphere in gradient balance with wind speed V_g. For a stationary TC vortex, analytic solutions for the height ($z_{\max}$) at which the supergradient jet is strongest [$1 + v(z_{\max})/V_g$] are given by K01 [cf. his (18), (24), and (27)]:

$$z_{\max} = \left(\sqrt{2K_m/|I|}\right)\tan^{-1}(-1 - 2/\chi), \tag{3a}$$

$$1 + v(z_{\max})/V_g = 1 + \left(\frac{\chi}{2\chi^2 + 3\chi + 2}\sqrt{\frac{\chi^2 + 2\chi + 2}{2}}\right) \times \exp[-\tan^{-1}(-1 - 2/\chi)], \tag{3b}$$

$$\chi = C_D V_g \sqrt{2/(K_m I)}, \quad \text{and} \tag{4}$$

$$I^2 = (f + 2V_g/R)(f + V_g/R + \partial V_g/\partial R), \tag{5}$$

where values of the arctangent function are between $\pi/2$ and $3\pi/4$, C_D is the drag coefficient, f is the Coriolis

[1] Consequently, the eddy viscosity in mesoscale models is anisotropic.

parameter, and R is the radius (distance from TC center). It is important to remember that K_m is a constant in this linear model. The ratio of the surface tangential wind to the gradient wind (or ''surface wind factor'') is shown by K01 [his (30)] to be a function of χ only.

With analytic solutions, the sensitivities of jet height and jet strength to individual changes in C_D, V_g, K_m, and R can be readily calculated (Fig. 1 of K01). The benefit of LES is that the interdependencies of these parameters are automatically considered (especially for K_m, which is diagnosed by LES) when determining the mean wind profile. As discussed in section 3 and the appendix, the present LES solves the governing equations in Cartesian coordinates, in which the effects of TC rotation are accounted for through modifying the Coriolis parameter.

b. The relevant case (an ''effective'' Ekman layer)

In Cartesian coordinates, the centrifugal force can be represented by a rotating reference frame. As explained in the appendix, the reference frame is a rotating cylinder (representing a TC) attached to the surface of a rotating sphere (representing Earth). What results is an ''effective'' Coriolis parameter—denoted f^*—that combines the rotations of the TC and Earth:

$$f^* = f + 2V_g/R, \tag{6}$$

where V_g is the rotational velocity of the TC. Thus, the important parameter is f^* rather than f. Because the second term on the RHS of (6) is defined to be nonnegative, $f^* \geq f$. Figure 1 shows f^*/f over a range of values of V_g and R with f corresponding to 34.5°N. For the sensitivity experiments considered in section 4, f^*/f ranges from about 8 (for $V_g = 35\,\mathrm{m\,s^{-1}}$ and $R = 120\,\mathrm{km}$) to 29 (for $V_g = 35\,\mathrm{m\,s^{-1}}$ and $R = 30\,\mathrm{km}$). This serves as a strong reminder that hurricanes are not in geostrophic balance with regard to Earth's rotation and that LES studies using a prescribed driving flow must account for the extra rotation.

The appropriate linear model—for a Cartesian Ekman layer, albeit with a much faster rate of rotation—replaces I in (3) and (4) with f^* (2475–2476 of K01).[2] Making these replacements, the depth De of the K01 partial-slip Ekman layer [the lowest level at which there is no cross-isobar flow; see chapter 5 of Holton (2004)] becomes

$$\mathrm{De} = (\sqrt{2K_m/f^*})\tan^{-1}\{-1/[1 + C_D V_g \sqrt{2/(K_m f^*)}]\} \tag{7}$$

with the same range of arctangent values as above. The present LES features an equation set that uses f^* instead of f, as detailed below.

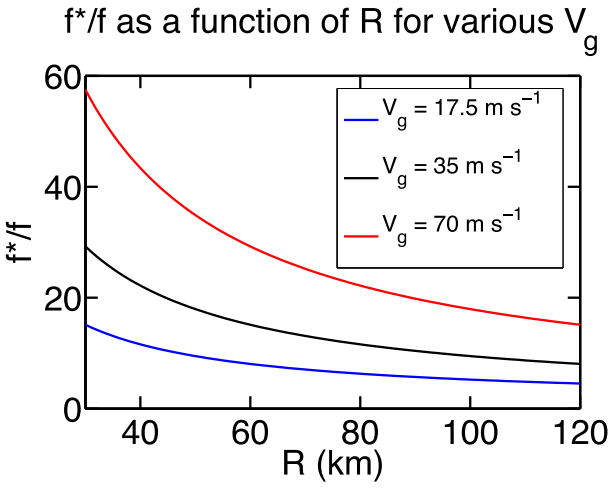

FIG. 1. Plots of f^*/f as a function of radius R (km) for selected values of V_g.

3. LES setup and results from control experiment

a. Model equations and configuration

The LES used for this study was developed at and is maintained by the National Center for Atmospheric Research (NCAR); readers are referred to Moeng (1984), Sullivan et al. (1994), and Sullivan and Patton (2011) for more details. The NCAR LES uses periodic lateral boundary conditions (LBCs); in addition, the flow is incompressible such that a Poisson equation for pressure can be solved (Sullivan et al. 1996). The resolved (denoted by overbars) momentum and thermodynamic equations can be written in vector form as (Sullivan and Patton 2011)

$$\frac{\partial \overline{\boldsymbol{v}}}{\partial t} + \overline{\boldsymbol{v}} \cdot \nabla \overline{\boldsymbol{v}} = -\mathbf{f}^* \times (\overline{\boldsymbol{v}} - \mathbf{V}_g) - \nabla \overline{\pi} + \mathbf{k} g \overline{\theta}/\theta_0 - \nabla \cdot \mathbf{T} \quad \text{and} \tag{8a}$$

$$\frac{\partial \overline{\theta}}{\partial t} + \overline{\boldsymbol{v}} \cdot \nabla \overline{\theta} = -\nabla \cdot \mathbf{B}, \tag{8b}$$

[2] Strictly speaking, our approach is using the Ekman limit for straight flow, except f is replaced with a (constant) f^*. K01 (p. 2475) notes that only the symmetric part of his solution reduces to the Ekman limit. Therefore, our LES setup cannot test the asymmetric part of K01's theory.

TABLE 1. Summary of various metrics averaged over the final 3 h of each LES run. The value of f^* for each simulation is calculated from (6). The approximate LES inertial oscillation periods were determined from u_* in Fig. 6. Jet strength is expressed as a percentage greater than V_g. The surface wind factor is the 20-m (lowest model level) tangential wind as a percentage of V_g. The theoretical inflow depths were calculated from (7) using values of K_m and C_D obtained from the LES experiments.

	Experiment	R30	CNTL	R120	V17.5	CNTL	V70	Charnock70	Land70
R (km)		30	60	120	60	60	60	60	60
V_g (m s^{-1})		35	35	35	17.5	35	70	70	70
z_0		(10)	(10)	(10)	(10)	(10)	(10)	(8) of GZ13	0.1 m
f^* (10^{-4} s^{-1})	[From (6)]	24.5	12.9	7.0	7.0	12.9	24.5	24.5	24.5
Period (min)	Theory	43.3	83.8	157.3	157.3	83.8	43.3	43.3	43.3
	LES	41.3	84.5	134.9	156.5	84.5	33.9	31.6	30.2
Jet strength (%)	LES	2.08	2.20	3.24	2.70	2.20	2.00	2.35	2.87
Jet height (m)	LES	220	420	620	260	420	460	580	700
Sfc wind factor (%)	LES	87.48	83.31	79.63	88.27	83.31	81.40	75.67	67.54
Inflow depth (m)	Theory	353	554	837	334	554	685	805	939
	LES	400	560	840	320	560	760	880	1040
z_i (m)	LES	736	836	931	422	836	1274	1465	1678

where $\overline{\pi}$ is the (periodic) pressure variable, $\overline{\boldsymbol{v}}$ the resolved wind vector, $\mathbf{f}^* = f^*\mathbf{k}$ with f^* given by (6) and $\mathbf{k}$ the unit vector in the z direction, $\mathbf{V}_g$ is the driving wind vector with speed V_g (see appendix) in the y direction that represents a geostrophic balance with the large-scale pressure gradient, g is the gravitational constant, and $\overline{\theta}$ is the virtual potential temperature (herein "temperature") with reference value θ_0. The subgrid-scale (SGS) fluxes and energy are

$$\frac{\partial e}{\partial t} + \overline{\boldsymbol{v}} \cdot \nabla e = \mathcal{P} + \mathcal{B} + \mathcal{D} - \mathcal{E}, \tag{9a}$$

$$\mathbf{T} = \overline{v_i v_j} - \overline{v}_i \overline{v}_j, \tag{9b}$$

$$\mathbf{B} = \overline{v_i \theta} - \overline{v}_i \overline{\theta}, \quad \text{and} \tag{9c}$$

$$e = (\overline{v_i v_i} - \overline{v}_i \overline{v}_i)/2, \tag{9d}$$

where e is the SGS turbulent kinetic energy (TKE), and ($\mathcal{P}$, $\mathcal{B}$, $\mathcal{D}$, $\mathcal{E}$) are the SGS TKE production, buoyancy, diffusion, and dissipation, respectively. As in Sullivan and Patton (2011), the SGS fluxes are calculated by the Smagorinsky scheme with constants $C_k = 0.1$ and $C_s \sim 0.18$. It is worth noting that this LES is a box-shaped domain in strict Cartesian coordinates and represents the turbulence statistics at a single, fixed radius R (as opposed to a radius interval).

The experiments are intended to follow the framework of NN12, albeit with a different treatment of the centrifugal force (see appendix). Wherever possible, the LES model parameters are set identical to those in NN12. These include grid spacing ($\Delta x = \Delta y = \Delta z = 40$ m), time step ($\Delta t = 0.1$ s), domain size ($500 \times 500 \times 100$ grid points; i.e., $20 \times 20 \times 4$ km^3), and Earth's Coriolis parameter f (corresponding to a latitude of 34.5°N). In addition, the initial temperature profile is set to $d\overline{\theta}/dz = 4$ K km^{-1} with surface temperature of 300 K; given the lack of an artificially strong capping inversion combined with periodic LBCs, the surface heat flux Q_* is set to zero[3] (as in NN12) to prevent the boundary layer from getting too close to the top of the LES domain. A radiative upper boundary condition was used following Klemp and Durran (1983). The horizontal wind field (u, v) is initialized as (0, V_g) everywhere. All of the LES runs (detailed in section 4) are integrated forward in time for 40 000 s (slightly over 11 h), and for analysis purposes layer-mean vertical profiles are averaged over the final 3 h, or 180 min, to remove the effects of the pseudo-inertial oscillation associated with f^* (for the cases with the slowest rotation, the oscillation period $2\pi/f^*$ is about 157 min; see Table 1).

b. Results from control experiment

The results from the sensitivity experiments (see section 4) are better understood in the context of a control simulation—herein called CNTL—of a strongly sheared, rapidly rotating boundary layer (i.e., a TC-like boundary layer). In CNTL, $R = 60$ km and $V_g = 35$ m s^{-1}; the surface drag C_D saturates at high wind speeds [following the results of Donelan et al. (2004)] and is calculated from a momentum roughness length

[3] Obviously, surface fluxes of sensible and latent heat are an essential part of the TC life cycle and should be included whenever feasible.

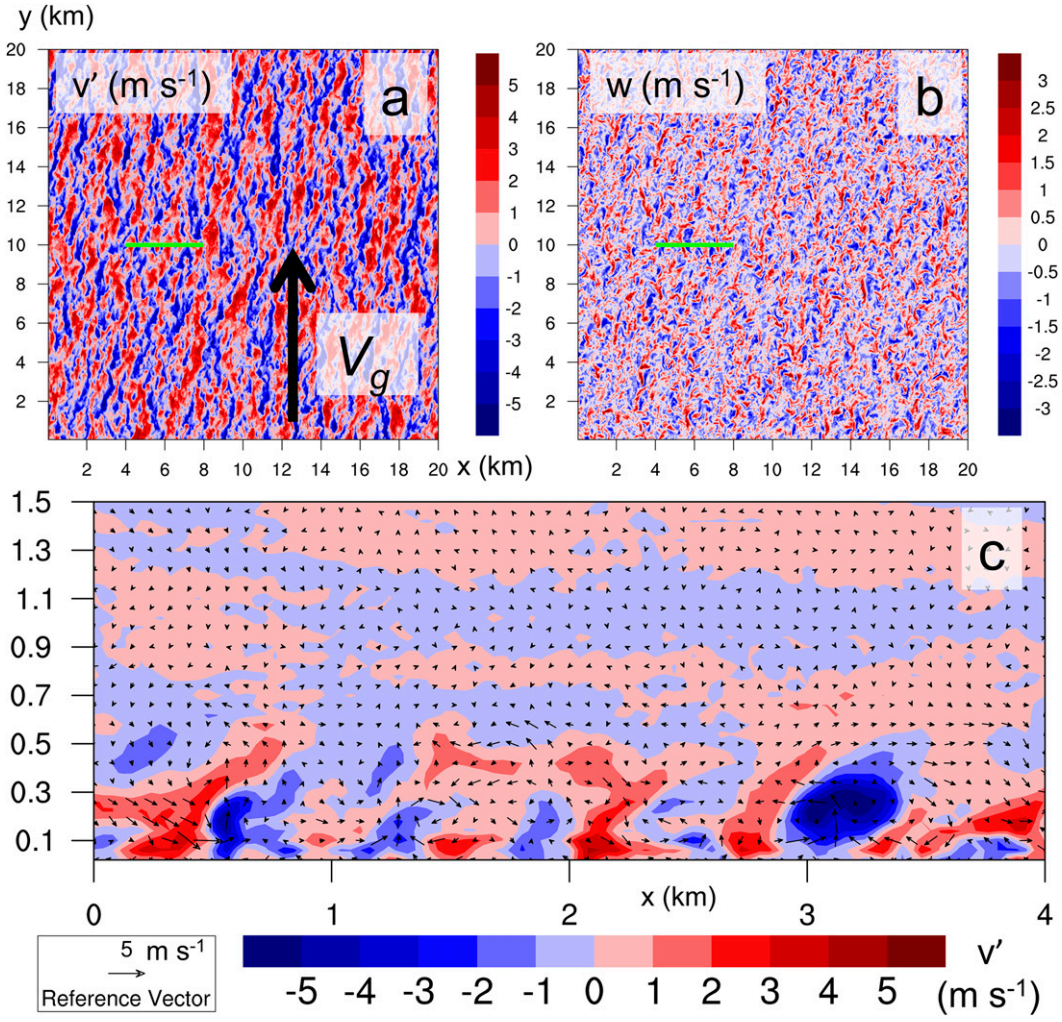

FIG. 2. Snapshots of instantaneous turbulent fluctuation velocity fields from the control LES run (CNTL) valid 40 000 s after the start of integration. (top) x–y plan views of (a) v perturbation at $z = 100$ m and (b) vertical velocity w at $z = 120$ m. The balanced wind V_g points in the y direction. The horizontal green lines show the location of the x–z vertical cross section in (c). (c) Fluctuations of v are color shaded and the along-section circulation (fluctuation u and w) is shown by arrows. Tick marks denote distances (km).

z_0 using (10) in GZ13, which is given here for completeness:

$$z_0 = \max\{1.27\times10^{-7}, \min[z_w z_2 + (1-z_w)z_1, 2.85\times10^{-3}]\}, \tag{10a}$$

$$z_w = \min\left[1, \left(\frac{u_*}{1.06}\right)^{0.3}\right], \tag{10b}$$

$$z_1 = 0.011\frac{u_*^2}{g} + 1.59\times10^{-5}, \tag{10c}$$

$$z_2 = \frac{10}{\exp(9.5u_*^{-1/3})} + \frac{1.65\times10^{-6}}{\max(u_*, 0.01)}. \tag{10d}$$

1) TURBULENCE STRUCTURE

It is worthwhile to show an example of the LES-resolved velocity fields (as in NN12). This is done in Fig. 2 for the CNTL run, valid 40 000 s after the start of the LES integration. The turbulent fluctuation (i.e., subtracting the horizontal average) tangential velocity v (Fig. 2a) at a height of 100 m above the ground shows coherent structures aligned nearly exactly with V_g (which is directed toward the top of the figure). The magnitudes of the turbulent fluctuations, however, are weaker than those found by NN12 (their Fig. 6), likely owing to a different surface drag [they used a land-based drag whereas this simulation uses the ocean-based Donelan-like drag in (10)]. A cross section that is nearly, but not exactly,

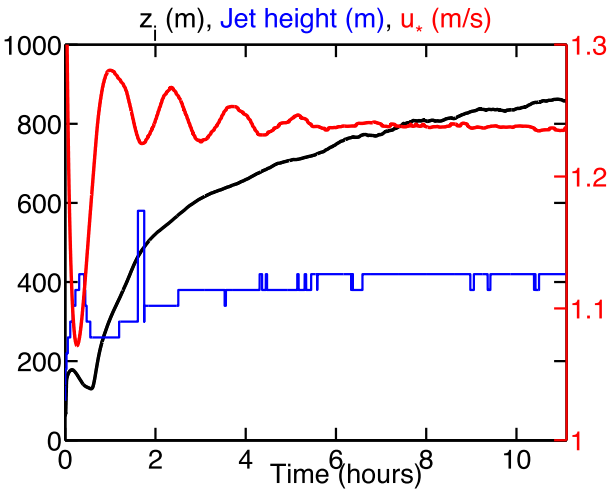

FIG. 3. Temporal evolutions of friction velocity u_* (red curve, $m\,s^{-1}$), jet height (blue curve, m), and thermodynamic boundary layer depth z_i (black curve, m) for the control LES run.

perpendicular to the roll axis (Fig. 2c) shows the strongest rolls extend to ~500 m above the surface. This result is qualitatively similar to the structures of some of the modes in NN12 (cf. their Figs. 12 and 13). A more detailed analysis of the boundary layer rolls is beyond the scope of the present research but warrants future attention.

2) TEMPORAL EVOLUTION

The temporal evolutions of the friction velocity u_*, thermodynamic boundary layer height z_i [calculated using the horizontally averaged level of maximum vertical gradient in temperature (Sullivan et al. 1998)], and jet height are shown in Fig. 3. A period of boundary layer spinup is apparent in both the u_* and z_i curves. After this initial spinup period, u_* quickly stabilizes to a nearly constant value of ~1.2 $m\,s^{-1}$, although there is an oscillation (with a period very close to the theoretical pseudo-inertial oscillation period of $2\pi/f^*$). In contrast, z_i increases throughout the simulation, representing continuous mixing and entrainment from the free atmosphere.[4]

3) QUASI-STEADY-STATE MEAN VERTICAL PROFILES

In the final 3 h of the LES integration, the boundary layer may be considered as quasi steady. Therefore, averages both horizontally (to remove transient turbulent fluctuations, denoted herein by angle brackets) and temporally (over this 3-h period, to remove the aforementioned inertial oscillation) can be taken to obtain vertical profiles of mean boundary layer quantities. These quantities—specifically, K_m (eddy viscosity),[5] temperature $\overline{\theta}$, and horizontal wind components (tangential v and radial u, both normalized by V_g)—are shown for CNTL in Fig. 4.

Because the LES explicitly resolves turbulence of the large, energy-containing eddies (unlike mesoscale models, which must parameterize all turbulence), the profile of K_m (Fig. 4a) is of particular interest. The increase in K_m from 20 $m^2\,s^{-1}$ near the surface to 40 $m^2\,s^{-1}$ at a height of ~200 m followed by the subsequent decrease back to 20 $m^2\,s^{-1}$ at a height of ~600 m is in line with the observational data of Zhang and Drennan (2012, their Fig. 8a). The temperature profile (Fig. 4b) is fairly straightforward (although not necessarily representative of actual TCs, as mentioned in footnote 4): a mixed layer in the lowest 600 m is capped by a strong inversion layer 400 m thick.

The vertical distribution of horizontal winds is a subject of considerable interest in the TC boundary layer for several reasons. Before stepped frequency microwave radiometer and GPS dropsondes, estimates of TC surface winds were often based upon observations above the boundary layer (Powell et al. 2009). Additionally, the overshooting jet is a key attribute of vortex dynamics (K01; Kepert and Wang 2001; Rotunno and Bryan 2012), and frictionally driven low-level inflow contributes to eyewall formation and replacement (e.g., Fang and Zhang 2012; Kepert 2013; Wang et al. 2013). The overshooting boundary layer jet ($\langle v\rangle/V_g > 1$) and frictionally reduced near-surface tangential winds are evident in Fig. 4c, as is the low-level radial inflow in Fig. 4d. As discussed in section 4, these features agree quantitatively with the linear theory of K01.

4. LES sensitivity experiments and comparison with K01 linear theory

a. *Boundary layer sensitivity in K01 linear model*

Similar to Fig. 1 of K01, the effects of C_D, V_g, K_m, and R on surface wind reduction and De are shown in Fig. 5 [using default values of $f = 8.26 \times 10^{-5}$ (corresponding to a latitude of 34.5°N), $C_D = 0.002$, $V_g = 35\,m\,s^{-1}$,

[4] It is important to remember that the LES used here does not account for surface heat fluxes and phase changes of water (both evaporation and condensation), all of which impact the thermodynamic properties of a real TC boundary layer. Therefore, z_i should not be compared with observations of the TC boundary layer (e.g., Zhang et al. 2011b).

[5] As discussed later, K_m—calculated from (1)—actually has two components: one associated with the turbulent fluxes resolved by the LES, the other associated with the subgrid-scale fluxes parameterized by the LES. In Fig. 4a, the sum of these two components is shown; Fig. 11a shows that the subgrid-scale contribution is minor above the surface layer.

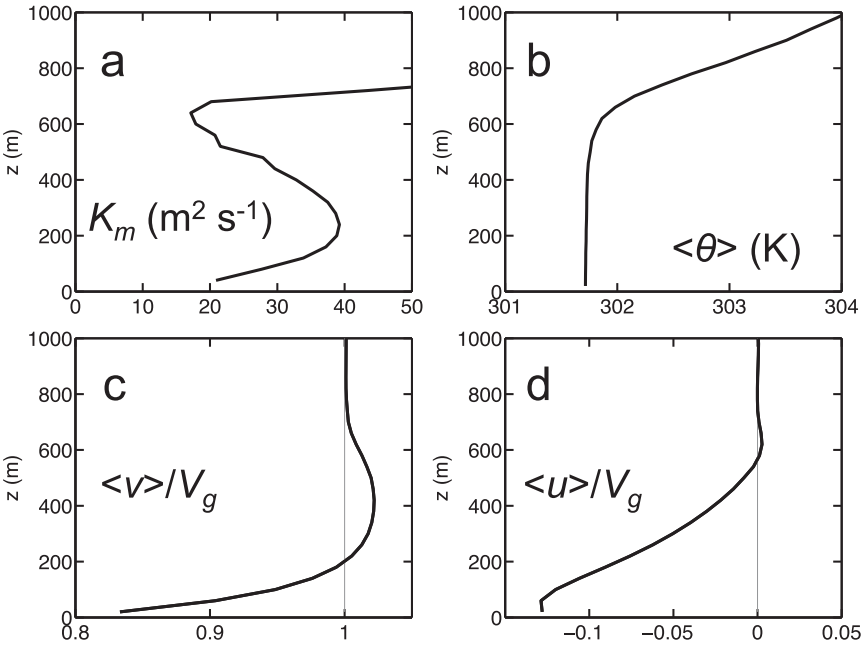

FIG. 4. Quasi-steady-state (averaged at each vertical level over the final 3 h of the control LES run) vertical profiles of (a) diagnosed turbulent diffusivity K_m (m^2 s^{-1}), (b) temperature (K), (c) tangential velocity v normalized by V_g, and (d) radial velocity u normalized by V_g.

$K_m = 50\,\mathrm{m^2\,s^{-1}}$, and $R = 60\,\mathrm{km}$]; readers are directed to Fig. 1 of K01 to see how the aforementioned four parameters impact jet strength and jet height. Of course, the assumption that these four parameters are all independent is incorrect (p. 2476 of K01): this was discussed earlier for K_m, but is also the case for C_D (e.g., GZ13 and references therein). Keeping this in mind when looking at Fig. 5 and Fig. 1 of K01, the LES

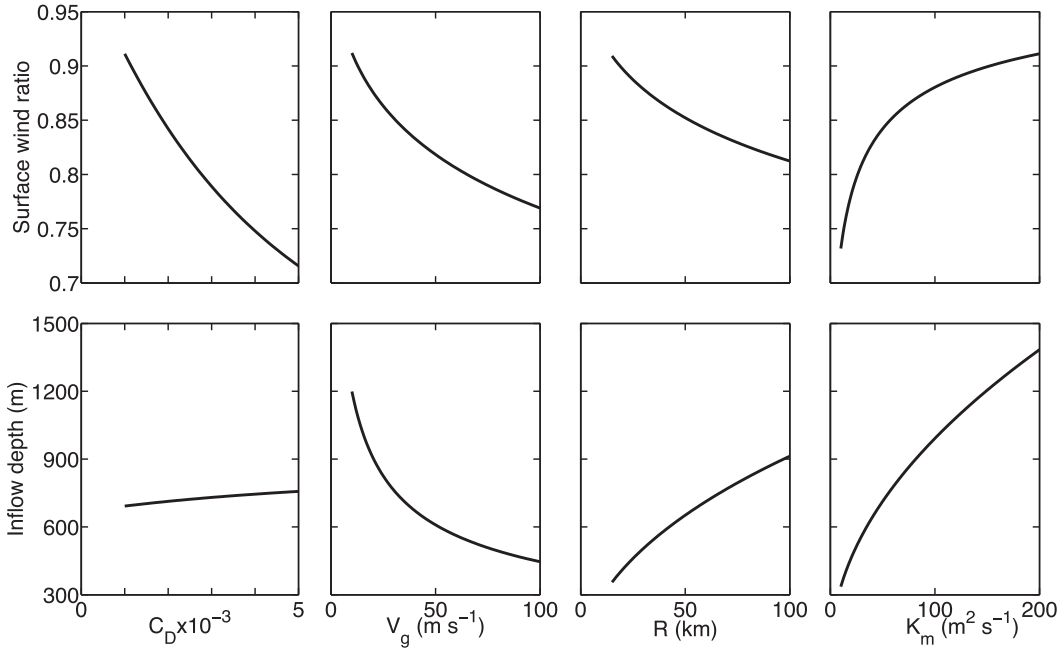

FIG. 5. Dependence of (top) surface wind reduction and (bottom) inflow-layer depth De on (left to right) surface drag coefficient C_D, balanced wind V_g, radius R, and turbulent diffusivity K_m in the linear partial-slip Ekman model of K01 (cf. his Fig. 1). Default (fixed) parameter values of C_D, V_g, R, and K_m are 0.002, 35 m s^{-1}, 60 km, and 50 m^2 s^{-1}.

sensitivity experiments are hypothesized to show that (i) the countereffect of K_m will result in the overshooting (supergradient) jet strength being essentially independent of C_D and V_g, but the jet will strengthen with R because eddy viscosity might not change much with radius; (ii) the jet height and inflow layer depth will increase with drag, radius, and possibly even wind speed (stronger winds will increase both C_D and K_m); and (iii) the ratio of surface tangential wind to balanced wind speed will decrease with C_D (a true first-order effect), V_g (increased V_g yields increased C_D, which could offset the counter effect of increased K_m), and R. These hypotheses hinge on how the LES diagnoses eddy viscosity.

b. *Overview of LES sensitivity experiments*

Section 3 established how a LES with periodic LBCs could represent a TC-like boundary layer—that is, a rapidly rotating, strongly sheared boundary layer. Now, in order to cover a multitude of possible TC environments, we examine the sensitivity of the results to changes in rotation rate (radius from TC center), wind speed, and surface drag. Unless explicitly stated, the sensitivity simulations have (R, V_g, and C_D) equal to the control simulation CNTL (60 km, 35 m s^{-1}, and "Donelan like" drag). As will be discussed in section 5, the present configuration of the NCAR LES does not include the nonlinear effects of large-scale horizontal gradients and vertical motions; the results shown below are thus best compared with the linearized model of K01.

1) SENSITIVITY TO ROTATION RATE (VIA R)

Looking at (6) and (8), one way to change the rotation rate f^*—without changing anything else—is by changing the radius from TC center R, with larger R corresponding to a slower rotation rate. In addition to the control simulation (CNTL, R = 60 km), LES runs with R = 30 and R = 120 km (named R30 and R120, respectively) are conducted to test the sensitivity to rotation rate. The rotation rate for each experiment is calculated from (6) and shown in Table 1.

2) SENSITIVITY TO V_g

Two simulations besides CNTL (V_g = 35 m s^{-1}) are run to test the effect of V_g on the LES: one with V_g = 17.5 m s^{-1} and another with V_g = 70 m s^{-1} (named V17.5 and V70, respectively). Looking at (6) and Table 1, changing V_g also changes the rotation rate f^*. Also note that the Donelan-like C_D curve ("Opt 2" in Fig. 1 of GZ13) saturates at a wind speed of ~33 m s^{-1}, which means that C_D is the same between CNTL and V70 but lower for V17.5.

3) SENSITIVITY TO C_D

The sensitivity of the LES results to parameterization of C_D is tested via three simulations (one of which is the Donelan-like drag curve used in all experiments above). The other two formulas used to determine C_D (converted to z_0 for use in the LES code) are a "Charnock like" formula and one with a constant z_0 = 0.1 m. The Charnock-like C_D formula is, as the name suggests, based on Charnock (1955) and increases monotonically with wind speed rather than saturating at hurricane-force winds [(8) of GZ13; "Opt 0" in their Fig. 1]. The C_D with a constant z_0 = 0.1 m was used in both NN12 simulations and represents the much rougher conditions over land. To provide more separation in C_D between the Donelan-like and Charnock-like simulations, we set V_g = 70 m s^{-1}. Therefore, the Charnock-like and land-based simulations are called Charnock70 and Land70, respectively, and are compared with V70 (which has the Donelan-like C_D).

c. *Results from sensitivity experiments*

To improve the flow and avoid repetition, this section is organized by feature (e.g., the characteristics of the overshooting jet), with the simulations grouped together. Specifically, the results are presented in the following order: temporal evolution (spinup, pseudo-inertial period, etc.), momentum fluxes (including the diagnosed K_m) and other turbulence characteristics, and the vertical profiles of the layer-mean horizontal wind components (including the jet, surface wind reduction, and inflow).

1) TEMPORAL EVOLUTION OF u_* AND Z_i

The time series of friction velocity u_* for each of the three experiments is presented in Fig. 6. Not surprisingly, u_* is most impacted by changes to V_g and to C_D (Figs. 6b,c). Friction velocity exhibits a slight dependence on the rotation rate (Fig. 6a), with faster rotation (smaller radius) translating to increased surface stress; this is in agreement with Kosović and Curry (2000, their Table 3). As in the control run, u_* exhibits a pseudo-inertial oscillation in all sensitivity experiments with a period that is comparable with the theoretical $2\pi/f^*$ (Table 1). The greatest departures from the theoretical period—of 20%–30%—occur at extreme winds (V_g = 70 m s^{-1}). NN12 also found oscillations in time series of u_* (their Fig. 1); the period of the oscillation increased with R.

The "cold start" nature of the LES [that is, the model was initialized with winds (u, v) = (0, V_g) everywhere] means that there is a time scale for the boundary layer to

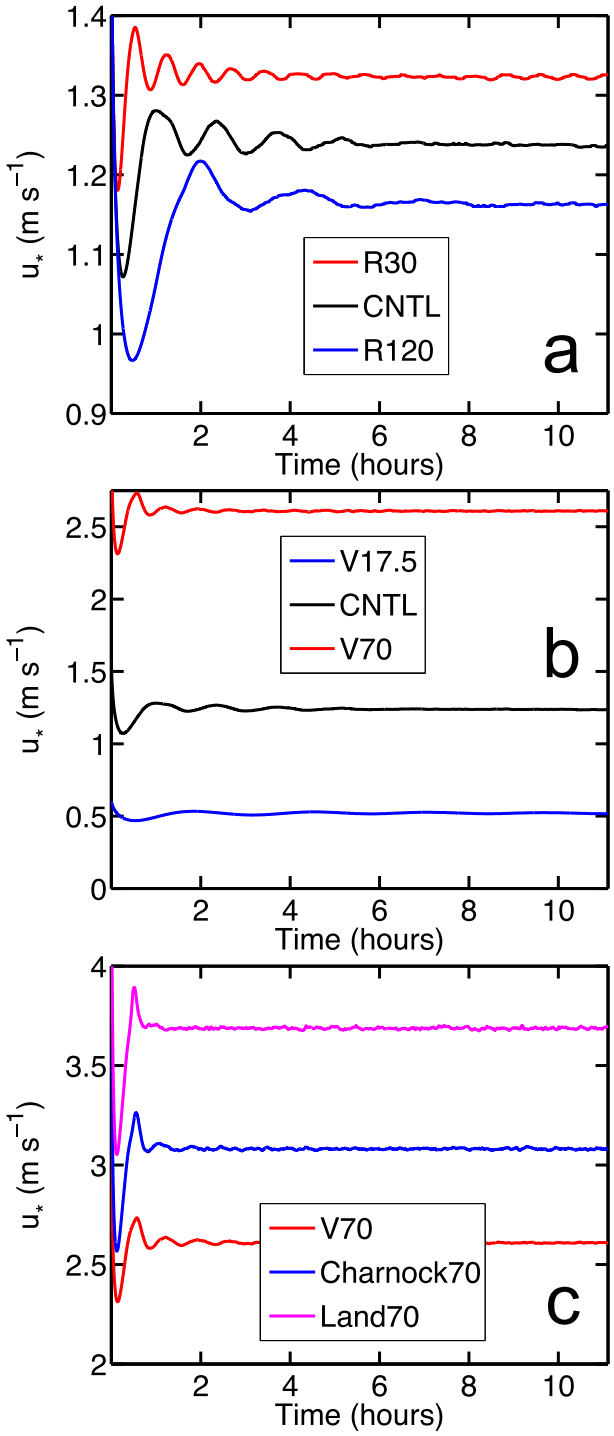

FIG. 6. Temporal evolution of u_* (m s^{-1}) for LES experiments testing the sensitivity to (a) rotation rate via radius R, (b) wind speed V_g, and (c) surface drag C_D. Note that some of the same LES runs (CNTL and V70) appear in multiple panels.

spin up; this is reflected in the initial sharp decrease in u_* and scales as $1/f^*$ (Eliassen and Lystad 1977). Note that changes to C_D (Fig. 6c) show little differentiation in oscillation period or spinup time, which is to be expected because drag does not affect f^*. The evolution of the thermodynamic boundary layer height z_i (Fig. 7) also exhibits a characteristic time scale for spinup. As with u_*, z_i is most impacted by V_g and C_D (Figs. 7b,c), such that larger values yield a deeper thermodynamic boundary layer. A slower rotation rate (increasing R) also raises the thermodynamic boundary layer height (Fig. 7a), which is consistent with observations and mesoscale simulations [e.g., Zhang et al. (2011b) and references therein].

2) MOMENTUM FLUXES VIA K_m AND OTHER TURBULENCE CHARACTERISTICS

As previously stated, the benefit of LES is that turbulence from the energy-containing eddies are explicitly resolved. To get a sense of the size of the turbulent eddies, two-dimensional power spectra [similar to the 1D spectra shown in Fig. 10a of Bryan et al. (2003)] for vertical velocity w at a height of 120 m were calculated by compositing output every 25 s for the last 5000 s of each simulation; the spectra are shown in Fig. 8. With the possible exception of V17.5 (Fig. 8b), all runs exhibit a region where the spectra follows a $-5/3$ power law, indicating that an inertial subrange is being resolved. Moreover, the wavelength of the spectral peak—that is, the characteristic size of the resolved energy-containing eddies—is ~600 m for all simulations. It should be noted that Wurman and Winslow (1998) observed TC boundary layer rolls over land with a similar characteristic wavelength, although Morrison et al. (2005) found typical roll wavelengths on the order of 1450 m.

Turbulent kinetic energy (TKE) and diagnosed vertical mixing length $\ell_v = \sigma_w^3/\varepsilon$ [where σ_w^3 is the cube of the standard deviation of w and ε is viscous dissipation of TKE; see p. 1451 of Zhang et al. (2011a)] averaged over the final 3 h are shown in Fig. 9 for each of the sensitivity experiments. As expected, increasing V_g and C_D significantly increases TKE (Figs. 9b,c), with values exceeding 40 J kg^{-1} for Land70. Moreover, TKE increases (slightly) with increasing R (Fig. 9a) for $V_g = 35$ m s^{-1}. TKE measurements away from the eyewall (i.e., in areas without extreme net vertical velocity) for winds 32–33 m s^{-1} at heights ~500 m [intervals 7–10 in Table 3 of Zhang et al. (2011a)] are on the order of 1.5–4 J kg^{-1}. For comparison, TKE at 500 m for R120 (Fig. 9a) is ~1.4 J kg^{-1}, which is a combined consequence of the idealized nature of the simulations (no buoyancy), differences in the vertical profiles of horizontal velocity, and

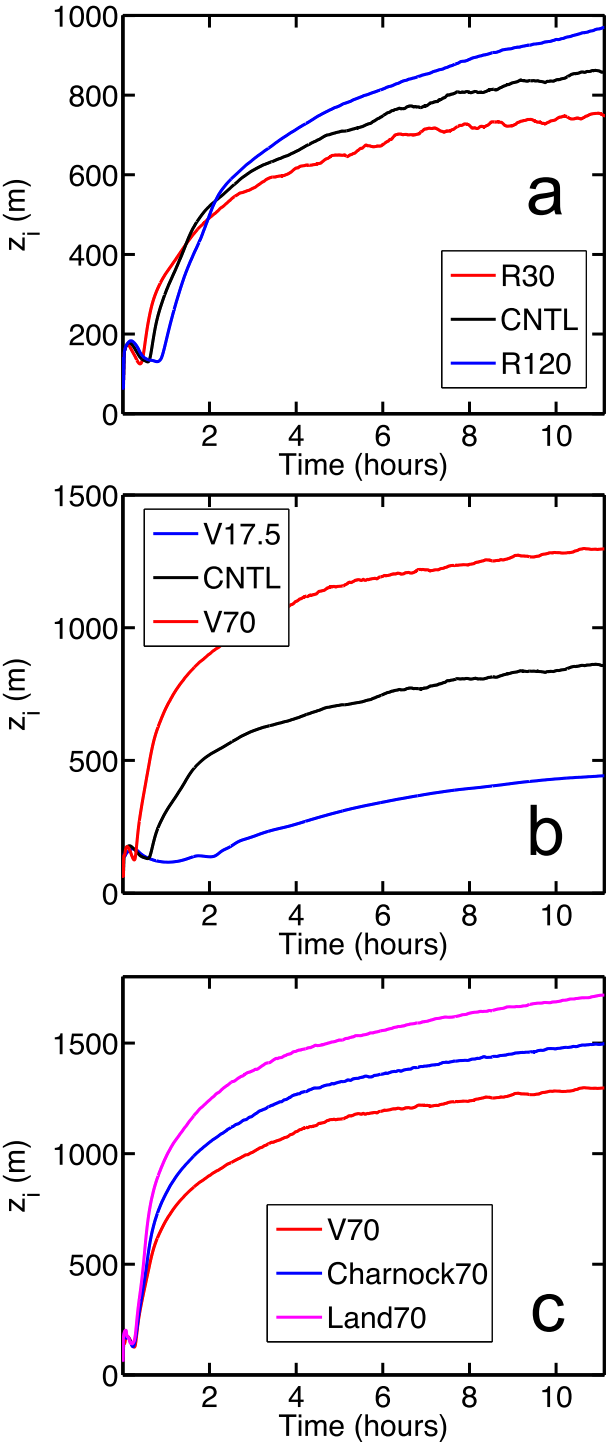

FIG. 7. As in Fig. 6, but for z_i (m).

observation errors. Looking at profiles of ℓ_v (Figs. 9d–f), it is clear that the calculated mixing length is essentially independent of R (f^*) and C_D (Figs. 9d,f) in the well-mixed part of the boundary layer and that ℓ_v increases with V_g (Fig. 9e). The ℓ_v values observed by Zhang et al. (2011a) corresponding to the abovementioned intervals 7–10 in their Table 3 range from 52.1 to 253.5 m; the LES-calculated ℓ_v at similar wind speed and height (35 m s^{-1}, 500 m) ranges from 150 to 191 m (Fig. 9d).

Recall that eddy diffusivity K_m (which contains a resolved-scale component and a subgrid-scale component) can be diagnosed via (1). The absolute values of the resolved- and subgrid-scale components of vertical momentum flux and the magnitude of the vertical wind shear (all averaged over the last 3 h of the simulations) are shown in Fig. 10, and the resultant K_m profiles [using (1)] are shown in Fig. 11. Looking at Fig. 10, both vertical momentum flux (and wind shear) change between experiments, with the most obvious—and unsurprising—result being that increased V_g and C_D yield stronger momentum fluxes and shear (Figs. 10b,c,e,f). Increasing R (slower rotation) yields a deeper layer of strong momentum fluxes owing to the deeper inflow layer De (cf. Table 1). When adding the resolved- and subgrid-scale components of vertical momentum flux for the experiments with $V_g = 35$ m s^{-1} (Fig. 10a) and assuming an air density of $\sim$1.25 kg m^{-3}, we obtain near-surface stress values between 1.5 and 1.75 N m^{-2}, which are remarkably similar to the TC boundary layer observations reported by Zhang and Drennan (2012, their Fig. 6a).

With the exception of V17.5 (Figs. 11b,e), the resolved component of K_m is substantially greater than the subgrid-scale component above the lowest 10% of the dynamic boundary layer, which indicates that the large-scale, energy-containing eddies are being explicitly resolved by this LES. A finer grid resolution is necessary to fully resolve the large turbulent eddies for V17.5 (because the resolved component of K_m is never much greater than the subgrid-scale component), but running all of the simulations (or even just V17.5) at higher resolution exceeds our computational constraints. Although it is doubtful that V17.5 is actually true LES, its inclusion (or exclusion) here does not change any of our conclusions.

Figure 11a shows that slower rotation (larger R) yields larger eddy diffusivity; nevertheless, the effects of R are substantially less than those of V_g (Fig. 11b), with stronger winds leading to larger K_m in the well-mixed part of the boundary layer. Not surprisingly, increasing surface drag (Fig. 11c) also increases K_m in the well-mixed part of the boundary layer.[6] Normalizing K_m by [u_*De] (Figs. 11d–f) is quite revealing. Changing V_g

[6] Toward the top of the boundary layer, and in the free atmosphere, the LES has very weak mean vertical wind shear. When calculating K_m from (1), shear appears in the denominator, leading to very large, but physically meaningless, values of eddy diffusivity above the well-mixed part of the boundary layer.

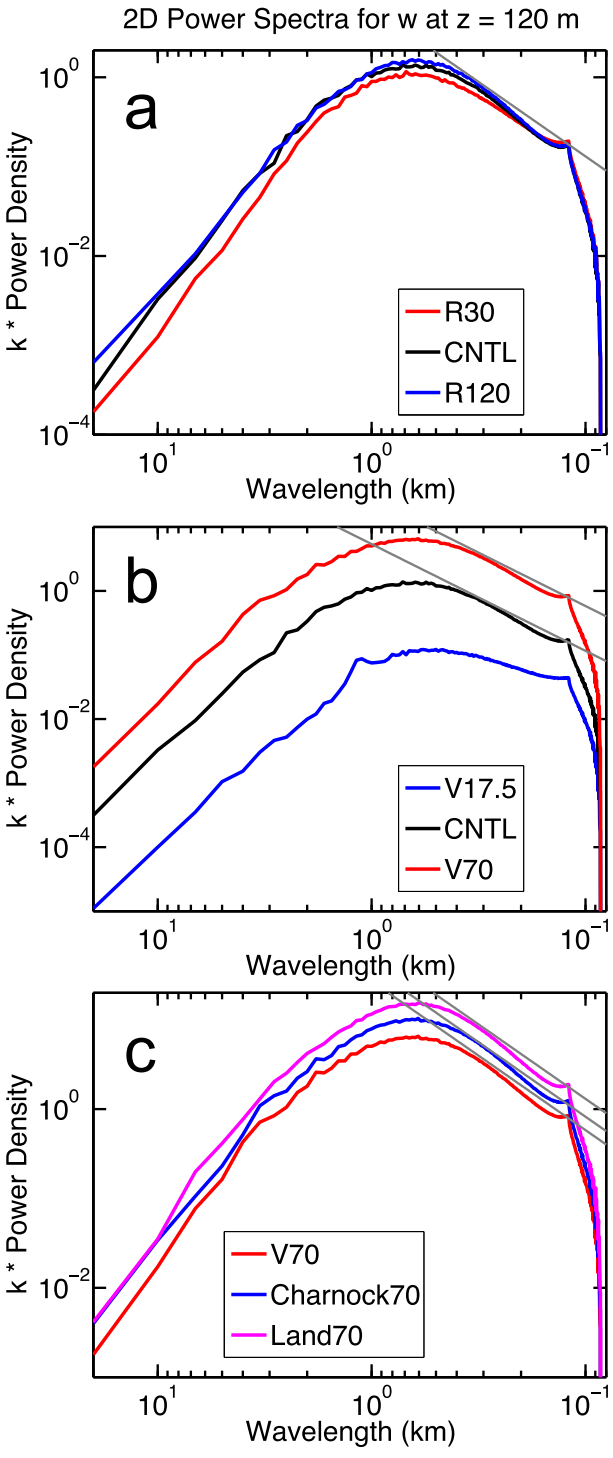

FIG. 8. Two-dimensional energy spectra (multiplied by wavenumber k) of vertical velocity w at a height of 120 m as a function of wavelength for the LES experiments. The thin gray diagonal lines show a $k^{-5/3}$ power law. Spectra were computed for each 25-s output interval in the last 5000 s and then averaged over that period.

(from 35 to 70 m s^{-1}) or surface drag (at 70 m s^{-1}) shows a general collapse of the normalized K_m curves (Figs. 11e,f). The feedback between K_m and parameters such as V_g—which linear models such as K01 are unable to represent—can account for the differences between the LES results and analytical solutions, as discussed below.

3) VERTICAL STRUCTURE OF LAYER-MEAN HORIZONTAL WIND

As in Figs. 4c and 4d, the quasi-steady-state mean profiles of normalized tangential and radial wind are shown in Figs. 12 and 13, respectively. An overshooting tangential wind jet develops in every single run, although the jet strength[7] and corresponding height vary from simulation to simulation (Table 1). Both the height and strength of the jet increase with increasing R (decreasing rotation rate; Fig. 12a), which is in agreement with the K01 linear model (Fig. 1 of K01); NN12 also show jet height to increase with R (their Fig. 3). Because V_g decreases with R beyond the radius of maximum winds, Fig. 12 suggests a strengthening jet (in a relative sense) outward of the inner core. More surface drag yields a higher and stronger jet (Fig. 12c and Table 1), consistent with K01 (Table 1 and his Fig. 1). The normalized jet strength for all simulations, while comparable with K01, is considerably weaker than observations and nonlinear models (e.g., K01; Kepert and Wang 2001), implying similarities between the LES and the K01 linear model. Nevertheless, there are some areas of disagreement between the two: increasing V_g in the LES yields a higher and relatively weaker jet (Fig. 12b and Table 1), opposite of the linear model (Fig. 1 of K01). The disagreement can be explained by the fact that K_m also increases with V_g (Fig. 11b), which overwhelms the direct effect of V_g captured by the linear model. An example of the interaction between different parameters is visualized in Fig. 14, which shows how jet strength and height in the linear model are impacted by simultaneous changes to both C_D and K_m (holding V_g and R constant). Each overlaid dot shows the average K_m within the well-mixed boundary layer for the corresponding C_D simulation (e.g., Fig. 11c). Note that increasing drag yields increased K_m in the LES (dots in Fig. 14), but that for jet strength (Fig. 14a) the effect of increasing C_D (stronger jet) outweighs the effect of increasing K_m (weaker jet). Such interaction between parameters—particularly for V_g and K_m—was realized by K01 (p. 2476), although his linear model is unable to quantify the countering effects.

[7] In this study, "jet strength" is always normalized by V_g, as expressed in (3b).

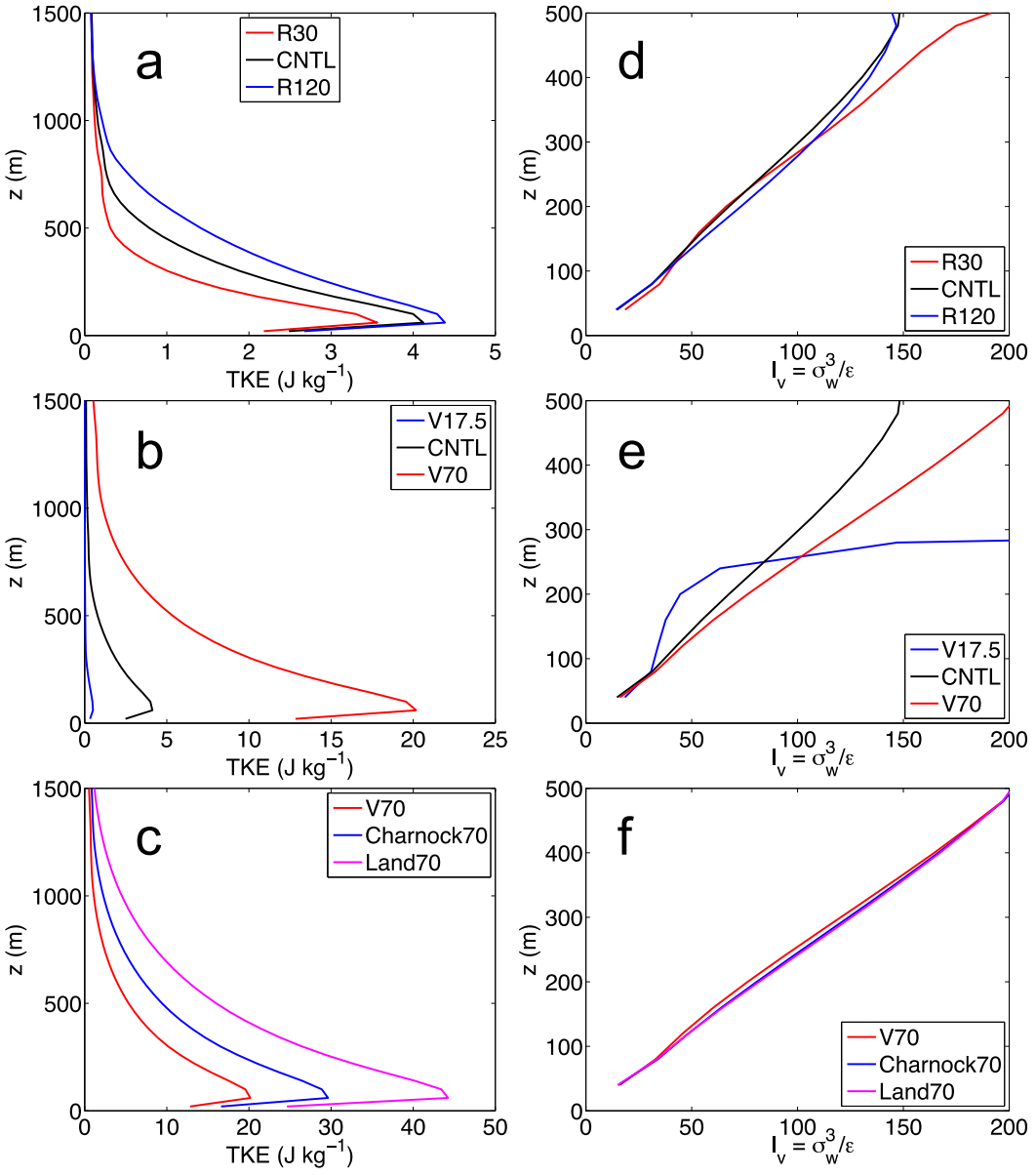

FIG. 9. Vertical profiles of (a)–(c) TKE (J kg^{-1}) and (d)–(f) diagnosed vertical mixing length ℓ_v (m; see text) for each of the LES experiments, averaged over the final 3 h of the simulations. Note that the abscissa and ordinate vary between panels.

The ratio of lowest model level (20 m) tangential wind to V_g (expressed as a percentage in Table 1) is most impacted by C_D (Fig. 12c). The decrease in near-surface tangential wind when going from ocean to land would favor an enhanced zone of low-level convergence along the coastline (Green et al. 2011). In all experiments, the LES results agree with the linear theory, with increases to R, V_g, and C_D all yielding decreases in near-surface tangential wind.

The radial wind profiles in Fig. 13 also have noteworthy features. Despite considerable frictionally driven inflow, there is essentially no outflow. This is because the periodic LBCs of the LES prevent both the low-level mass convergence and the net ascent that are characteristic of all tropical cyclones (see section 5). Still, there are some areas of agreement with observations, linear theory, and modeling studies. Most obvious is that increased C_D results in a stronger and deeper inflow layer (Fig. 13c); that is, higher drag further disrupts the balanced flow, causing near-surface winds to turn more toward lower pressure (e.g., Montgomery et al. 2010; GZ13; Green and Zhang 2014; Smith et al. 2014). A stronger (both

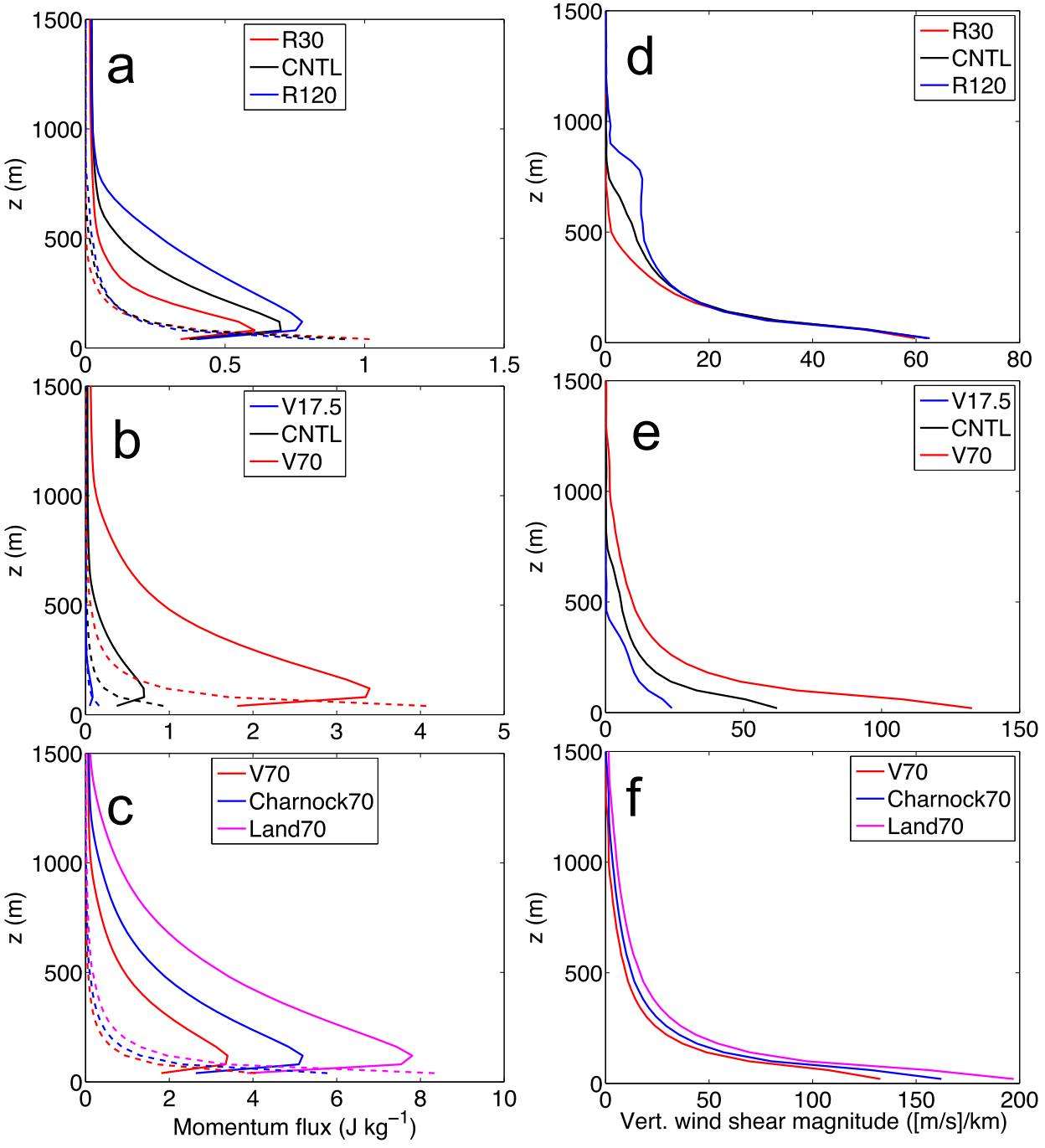

FIG. 10. As in Fig. 9, but for profiles of (a)–(c) vertical momentum flux magnitude [J kg^{-1}; resolved (subgrid)-scale components are shown by solid (dashed) lines] and (d)–(f) magnitude of vertical wind shear ($m\,s^{-1}\,km^{-1}$). Note that the abscissa varies between panels.

relatively and absolutely) inflow is also found with a stronger V_g (Fig. 13b). In addition, faster rotation (smaller R) results in a weaker and shallower inflow layer (Fig. 13a); NN12 found the inflow depth to increase with R (their Fig. 3). Consequently, an area of the storm in which V_g is nearly constant with radius will have low-level mass convergence, which could promote secondary eyewall formation (Kepert 2013; Wang et al. 2013). However, increasing V_g in the LES results in a deeper inflow layer (Fig. 13b), counter to what is predicted by the linear model (Fig. 5). As before, this disagreement is a consequence of increasing V_g leading to a higher K_m; in the linear model, increased K_m yields a deeper inflow layer (Fig. 5).

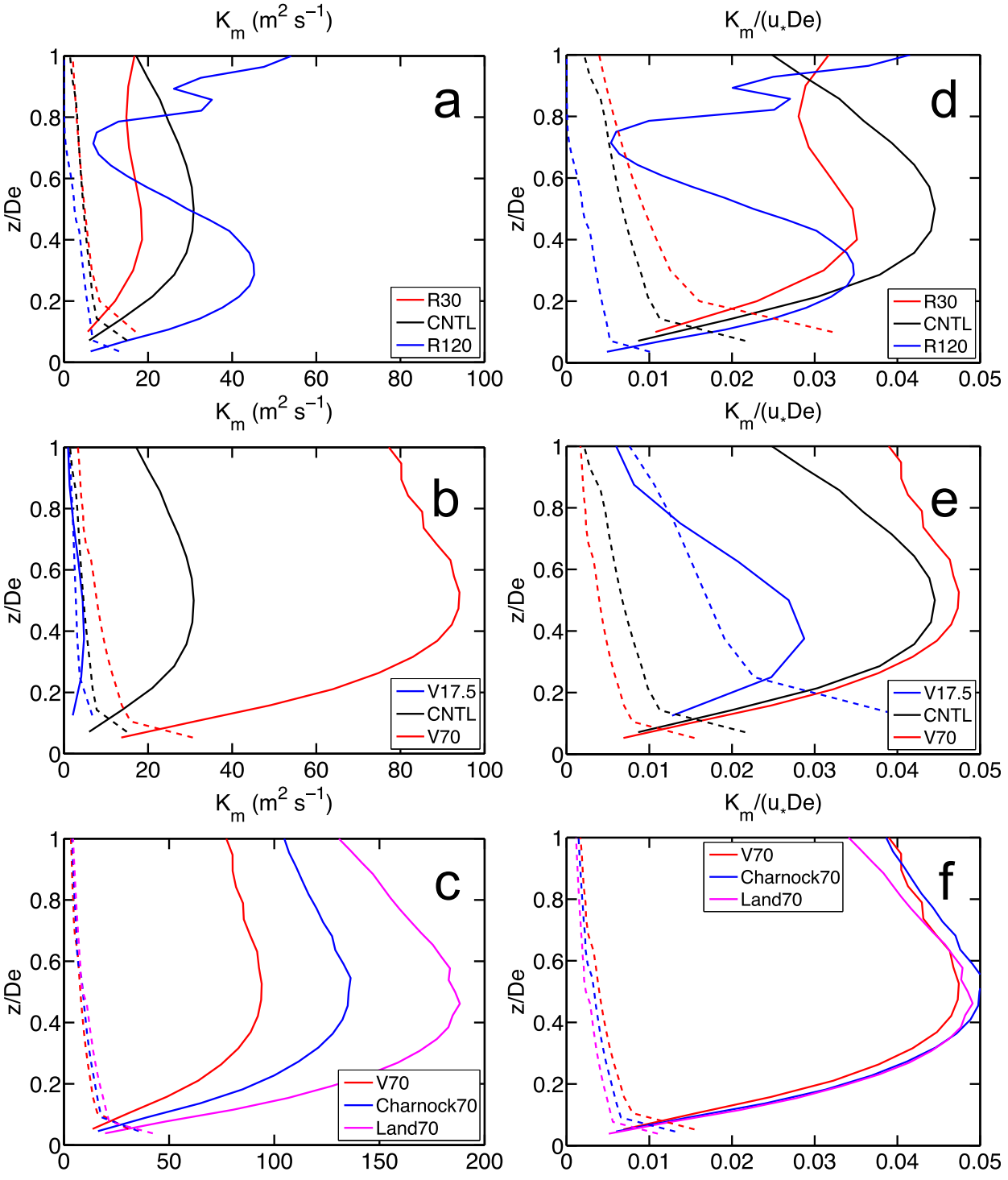

FIG. 11. Vertical profiles (normalized by De) of (a)–(c) the quasi-steady-state turbulent diffusivity K_m ($m^2 s^{-1}$) and (d)–(f) K_m normalized by u_*De from resolved-(solid lines) and subgrid-scale (dashed lines) turbulent fluxes for the LES sensitivity experiments. Note that the scale of the abscissa varies between panels.

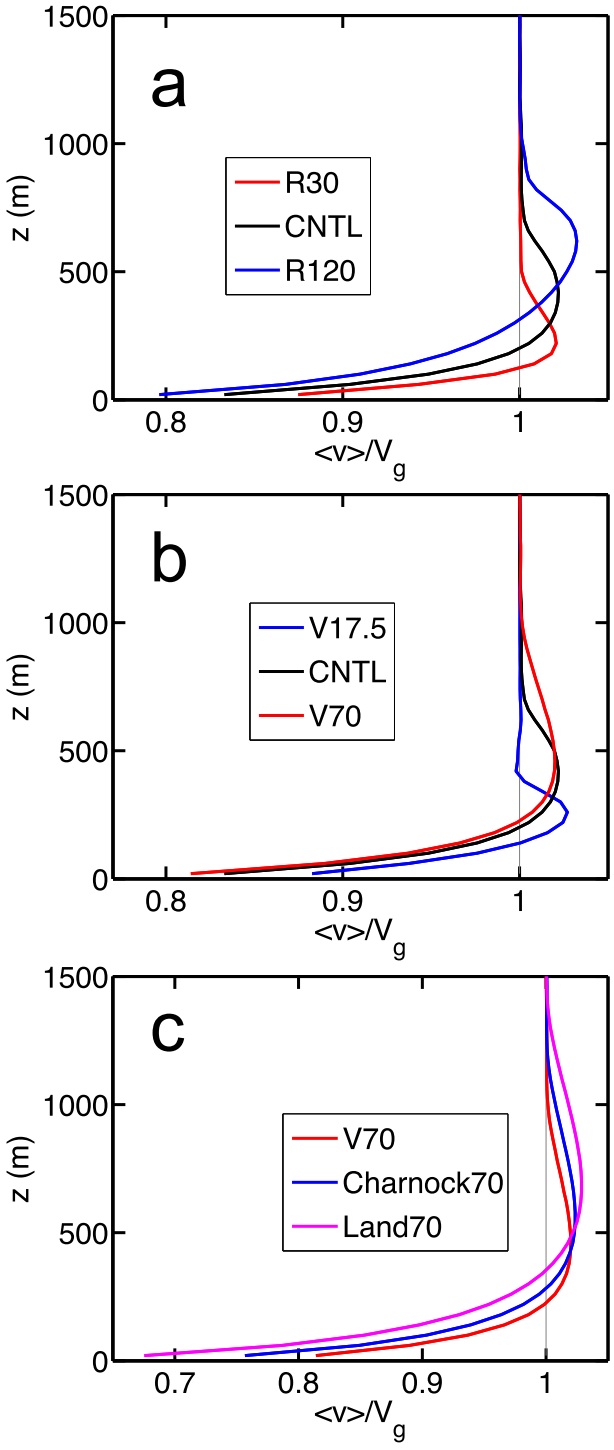

FIG. 12. As in Fig. 9, but for vertical profiles of tangential velocity v normalized by V_g.

There are several definitions for the depth of the TC boundary layer, based on either the thermodynamic or dynamic fields (Zhang et al. 2011b). Section 4b showed (Fig. 7) the temporal evolution of a thermodynamic boundary layer depth defined as the height of maximum vertical gradient of temperature; the quasi-steady-state boundary layer depth (averaged over the final 3 h of the LES runs) is considered here. A dynamic depth of the Ekman layer (defined as the lowest height at which there is no cross-isobar flow) for the partial-slip linear model of K01 is given by (7) in section 2. Table 1 also compares this theoretical Ekman-layer inflow depth[8] with the LES inflow depth and the LES thermodynamic depth z_i. There are two noteworthy points. First, there are substantial differences between the dynamic and thermodynamic boundary layer depths of the LES runs, consistent with the composited observations in Zhang et al. (2011b); as stated earlier, z_i is significantly larger than what is observed in real TCs because our simulations have a highly unrealistic thermodynamic structure. Second, the "theoretical" inflow depth is remarkably similar to the LES inflow depth, which reinforces the notion that this LES is representing a simple Ekman layer.

5. Discussion

Configuring the periodic LES to model the boundary layer of a horizontally homogeneous background state invites a comparison with Ekman layer theory. It was shown in section 2b that the LES models a boundary layer in an "effective" balance with f^* (as opposed to f), which for the linear model of K01 means that I is replaced by f^*. Because f^* is a function of V_g and R, the resulting partial-slip Ekman spiral solutions can still be compared with Fig. 1 of K01, albeit with his x parameter set to 1.

The qualitative and quantitative agreement between linear Ekman models and the LES is promising (including the exception where the effects of K_m overwhelm the effects of V_g), and it is tempting to apply the LES results to real TCs. Before doing so, however, the limitations of this idealized set of experiments must be fully understood, and what (if anything) could be done to conduct more realistic LES simulations. One limitation of the LES used here is that only dry processes are considered: latent heat release due to condensation of water vapor—which is fundamental for TC energetics (e.g., Emanuel 1986)—is neglected. Accounting for the phase changes of water vapor, as well as other physical processes including cloud microphysics (e.g., Nakanishi 2000) and radiative transfer, should be considered for future LES studies. A recent series of papers by Shpund

[8] Equation (7) requires a value of K_m; here, the average K_m in the boundary layer from the LES (see section 4b) is used to calculate (7). Calculating a truly "theoretical" Ekman depth requires an a priori constant value of K_m.

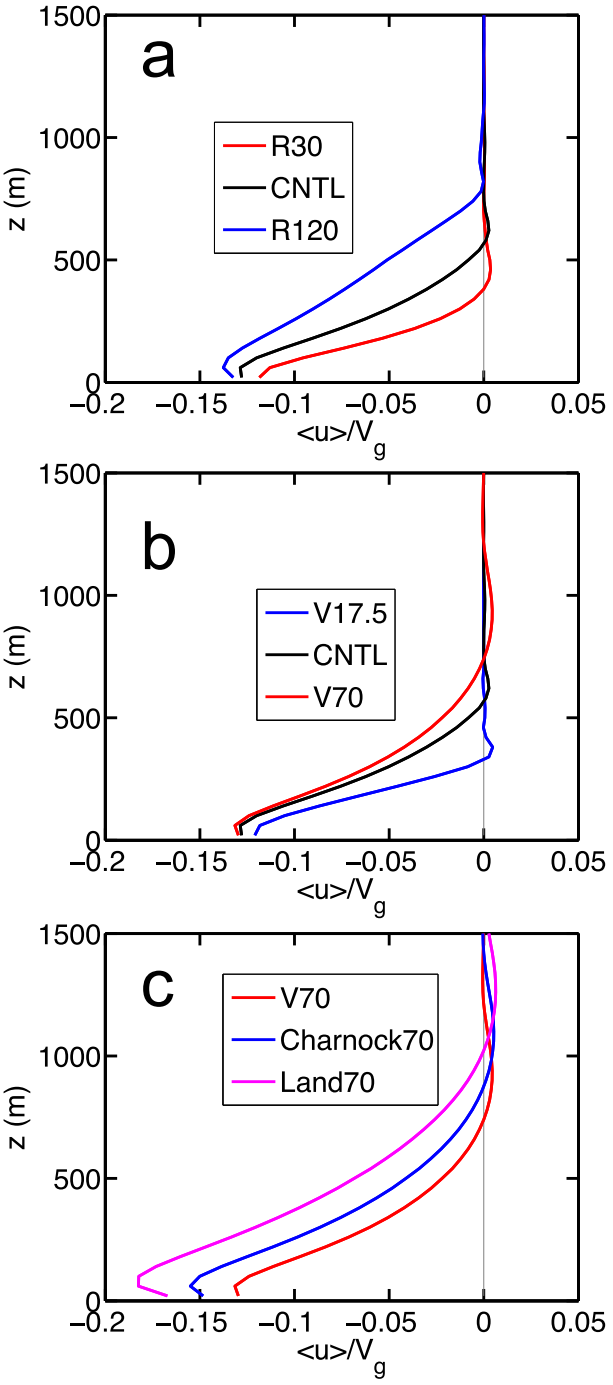

FIG. 13. As in Fig. 12, but for radial velocity u normalized by V_g.

et al. (2011, 2012, 2014) used a two-dimensional hybrid Lagrangian–Eulerian model (which is not actually LES) to investigate the effects of sea spray on the thermodynamics and microphysics of a turbulent TC boundary layer; their vertical velocity variance (Fig. 4 of Shpund et al. 2011) exhibits a stronger but more shallow profile than the LES runs in this study (not shown), while their energy spectra (Fig. 5 of Shpund et al. 2011) do show a −5/3 power law as a consequence of the velocity harmonics.

Another, more severe, limitation is that this Cartesian LES has periodic LBCs. With periodic LBCs, the net vertical velocity at each level must be exactly zero to satisfy incompressible continuity. Because of computational limitations that will become evident in the next paragraph, the present study applies periodic LBCs with a horizontally homogeneous mean pressure gradient (i.e., driving flow) and (initially) horizontally homogeneous temperature field. Doing so prohibits consideration of large-scale (i.e., mean flow) horizontal gradients, except for the nonperiodic component of the pressure in balance with some wind. For many atmospheric applications, including a horizontally homogeneous boundary layer driven by a free atmosphere in geostrophic balance (i.e., away from centers of high or low pressure), such LES experiments are frequently used (e.g., Moeng and Sullivan 1994; Beare et al. 2006). However, substantial gradients in the tangential and radial components of the mean flow, as well as nonnegligible vertical velocities, are essential features of TCs. When these features are neglected, as is the case for both the K01 linear model and the present LES, the strength of the overshooting jet is severely underestimated (Kepert and Wang 2001). Furthermore, the periodic, horizontally homogeneous LES means that if a nonzero surface heat flux is prescribed, then a strong capping inversion must also be specified to prevent the boundary layer from growing too deep and approaching the top of the LES domain. This becomes a problem in TCs, where there can be considerable surface heat flux. To prevent the boundary layer from reaching the top of the LES domain, we follow NN12 and set the surface heat flux to zero. As detailed in the concluding section, more realistic LES for TCs (that is still computationally feasible) will require a model without periodic LBCs.

With periodic LBCs, it is possible to account for large-scale horizontal wind gradients and vertical velocities,[9] as well as nonzero surface heat fluxes. To do so, an extremely large domain would be configured such that there is a significant amount of "buffer room" between the boundaries and the primary TC circulation of interest. Such an approach is feasible when computational costs are low: for example, Rotunno and Klemp (1982, p. 142) ran a periodic LBC cloud model with 32 × 32 ($\sim 10^3$) horizontal grid points but limited their analysis

[9] The net vertical velocity at each layer would still be zero, but there would be substantial room (in the eye and at very large radii) for compensating subsidence.

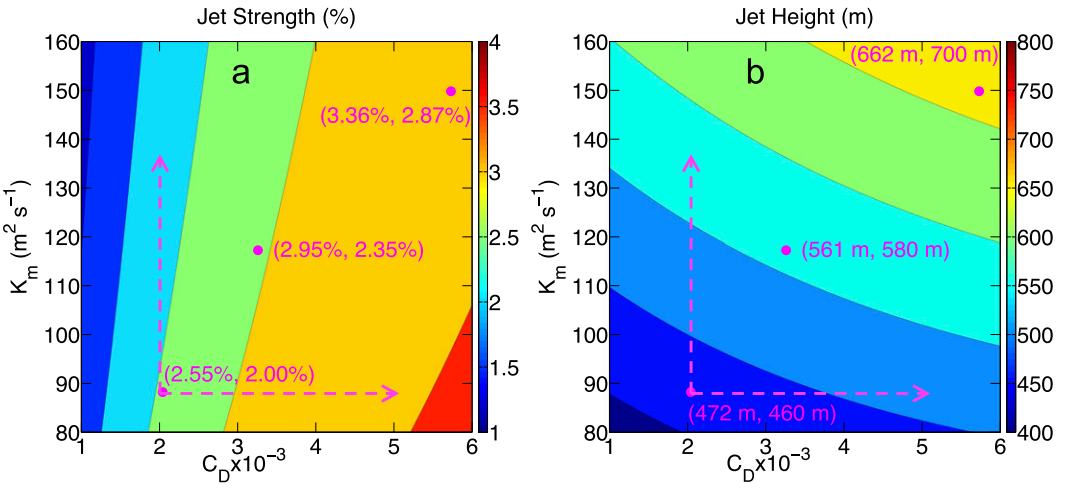

FIG. 14. Effect of both C_D (abscissa) and K_m ($m^2\,s^{-1}$, ordinate) on (a) jet strength and (b) jet height (shading denoted by colorbars) for the linear Ekman model in Fig. 5 (using the same values for R and V_g). Pink dots show the LES-determined values of C_D and K_m (averaged over the final 3 h of integration) for V70, Charnock70, and Land70: increased drag leads to increased K_m. The first number in parentheses in (a) is the jet strength [jet height in (b)] calculated from the linear model using the corresponding C_D and K_m values; the second number in parentheses in (a) is the jet strength [jet height in (b)] from the LES run (cf. Table 1). The dashed arrows show how jet strength and jet height in the linear model will change with independent changes to either C_D (horizontal arrow) or K_m (vertical arrow); cf. Fig. 1 of K01.

to a subregion comprising the center ~1/9 of the domain. This method is desirable because complex flows with large-scale horizontal gradients (away from the boundaries) can be modeled. Running a periodic LES of a TC with such a configuration would require a domain on the order of $1000 \times 1000\,km^2$ with horizontal grid spacing of under 100 m, which translates to 10^8 horizontal grid points; accounting for the vertical dimension increases the computational domain by another two to three orders of magnitude. Besides, at that grid size, one might as well run a "full-physics" nonperiodic LES (e.g., Rotunno et al. 2009). In any event, computational constraints render these approaches unfeasible at present.

How to include the centrifugal force in a Cartesian LES with periodic LBCs is not obvious at first glance. Perhaps the most naïve approach is to neglect the centrifugal force entirely and assume geostrophic balance—after all, the nonperiodic part of the pressure field is assumed to be in balance with some constant wind, so why not set that balanced wind speed equal to a realistic value observed in the free atmosphere of a TC (i.e., V_g)? The problem with this naïve approach is that TC boundary layer dynamics are often discussed in terms of angular momentum, which is a function of both wind speed and radius (e.g., K01; Rotunno and Bryan 2012). More importantly, Fig. 1 shows that the TC rotation is much stronger than the effects of Earth's rotation.

Recently, NN12 (following Foster 2005) attempted to account for the effects of curvature by approximating the conversion from cylindrical to Cartesian coordinates; unfortunately, as discussed in the appendix, approximations are made before taking derivatives, which introduces an unphysical instability in the barotropic vorticity equation. In contrast, the method used in this study—representing TC rotation as an "effective" Coriolis force by changing the rotating frame of reference—exactly conserves barotropic vertical vorticity. For completeness, additional LES experiments were run to test various representations of the centrifugal force. Specifically, the effect of using V_g (as opposed to the horizontal averaging in NN12) and the factor of 2 in the $1/R$ term (not included in the NN12 equations) were considered. The difference between V_g and the NN12 equations was mostly negligible, except that use of the latter yielded a somewhat stronger inflow in the lowest ~300 m (Fig. 15b). The factor of 2 proved to be much more significant; this was already demonstrated when looking at the sensitivity to rotation rate (via R), with the R120 simulation being equivalent to dropping the factor of 2 from the $1/R$ term. Subject to the limitations described two paragraphs above, the present treatment of the centrifugal force is most appropriate for a Cartesian LES (with a horizontally homogeneous mean pressure gradient) with periodic LBCs.

It may be tempting to compare the results of these LES runs with results from TC boundary layer studies that use mesoscale simulations. One major issue is that most of these mesoscale simulations consider the two-way feedback between the moist boundary layer and free atmosphere in the evolution of a TC (e.g., Braun

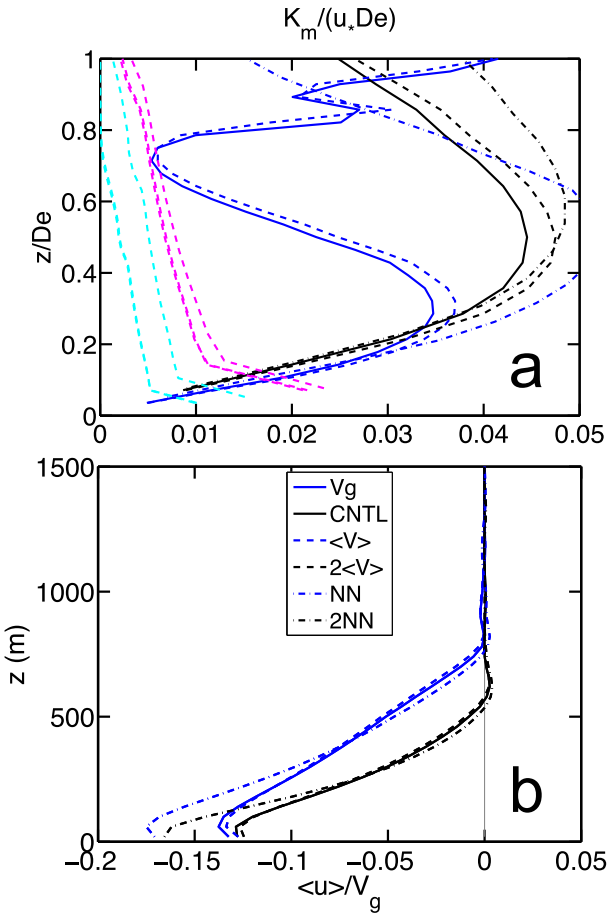

FIG. 15. (a) Vertical profiles (normalized by De) of resolved (blue and black) and subgrid-scale (cyan and magenta) K_m (normalized by u_*De), and (b) vertical profiles of mean radial velocity $\langle u \rangle$ (normalized by V_g) for various representations of streamline curvature. The simulations are named as follows: Vg (CNTL) uses $f^* = f + V_g/R$ ($f^* = f + 2V_g/R$); $\langle V \rangle$ ($2\langle V \rangle$) uses $f^* = f + \langle V \rangle / R$ ($f^* = f + 2\langle V \rangle / R$), where $\langle V \rangle$ is the horizontally averaged V at each level of the LES; NN uses the exact same formulas as NN12 [their (1) and (2)]; and 2NN replaces all $1/R$ terms by $2/R$ [cf. (6)].

and Tao 2000; Bryan 2012; Gopalakrishnan et al. 2013), whereas the LES described here examines the response of a (highly idealized) boundary layer to the strong shear and rapid rotation characteristic of a TC. The simulations of Kepert and Wang (2001) and Kepert (2010, 2012) do consider the dry boundary layer response to a constant external forcing and thus warrant comparison with the LES results. In particular, the vertical distribution and magnitudes of K_m in Kepert's (2012) Louis scheme (his Fig. 3g) and higher-order boundary layer scheme (his Fig. 6g) are somewhat similar to K_m in CNTL and R120 (Fig. 8a). In fact, another possible avenue of future research may be to adapt a diagnostic model similar to that detailed in Kepert and Wang (2001) to LES resolution.

6. Concluding remarks

A Cartesian LES with periodic LBCs was used to investigate the impacts of rotation rate (via radius from TC center), background wind speed, and surface drag on the evolution and quasi-steady state of a TC-like planetary boundary layer. The centrifugal force of the TC was incorporated into the LES equations through an "effective" Coriolis parameter f^*, which does not introduce any unphysical instability into the barotropic vorticity equation (unlike a previous study by NN12). Therefore, researchers who want to investigate the TC boundary layer with a periodic Cartesian LES should consider using the f^* set of equations rather than those used by NN12.

The LES used here does not account for large-scale (mean flow) vertical motions or horizontal velocity gradients, which means that the present results are best compared with a linear partial-slip Ekman model developed by K01. Reassuringly, several of the LES results are consistent with the linear model. For example, decreasing the rate of rotation (increasing distance from TC center) and increasing surface drag result in a stronger and higher overshooting (supergradient) jet in the boundary layer, a weaker near-surface tangential wind, as well as a deeper inflow layer. When the balanced (driving) wind speed V_g was increased in the LES, however, there was a weaker, higher jet and a deeper inflow layer—opposite of what was predicted by linear theory. Such a result is explained by the concomitant increase in turbulent diffusivity K_m, which in the linear theory acts opposite to, and in the LES overwhelms, the direct effect of V_g. The inflow-layer depths of the LES runs were remarkably close to the "theoretical" depths calculated from the K01 linear model. An unexpected finding is that K_m decreased with an increasing rotation rate (the a priori belief was that K_m was independent of rotation). In addition, the effective Coriolis parameter was evident in the time series evolution of friction velocity in two ways: as an inertial oscillation with a period close to the theoretical $2\pi/f^*$ and as a spinup period with a time scale of $1/f^*$ [following Eliassen and Lystad (1977)].

The limitations of using a Cartesian LES with periodic LBCs to study the TC boundary layer were discussed. Such a LES ideally would have a horizontal domain area on the order of $1000 \times 1000\,\text{km}^2$—computational constraints preclude this configuration in the near future. Consequently, a periodic Cartesian LES must be set up with a horizontally homogeneous driving flow. The main problem with this approach is that nonlinear advection by gradients in the mean flow—which are important for the dynamics of the TC boundary layer (Kepert and Wang 2001)—cannot be captured. Therefore, alternative methods should be considered to study the turbulence of

the TC boundary layer and compared with the results shown here. Despite the limitations of the present LES setup, there was agreement with observational results: the size of the boundary layer rolls (~600 m) was similar to that found by Wurman and Winslow (1998); moreover, surface stress values were remarkably close to observations by Zhang and Drennan (2012). The most attractive alternative to the present idealized numerical setup is to insert nested LES domains inside a mesoscale simulation. This has been done for the Weather Research and Forecasting (WRF) Model on few occasions, including a study of PBL turbulence along the coastline ahead of a landfalling TC (Zhu 2008) and a demonstrative proof-of-concept simulation (Rotunno et al. 2009). We have recently run WRF-LES experiments for a real TC case (Hurricane Katrina in 2005); these WRF-LES simulations use full moist physics and exhibit small-scale turbulent structures for horizontal grid spacings between 1/3 and 1/9 km (Green and Zhang 2015).

Acknowledgments. This material is based upon work supported by a National Science Foundation (NSF) Graduate Research Fellowship under Grant DGE-1255832. Additional support is provided by ONR Grant N000140910526, NSF Grants AGS-0840651 and 1305798, and the Graduate Visitor Program (GVP) at the National Center for Atmospheric Research (NCAR). We are indebted to Peter Sullivan, Rich Rotunno, and George Bryan for countless conversations and suggestions on this research. Dr. Sullivan is also thanked for providing the NCAR LES code and for hosting the lead author for the GVP. Dr. Chun-Chieh Wu and three anonymous reviewers provided beneficial comments that helped improve the manuscript. We are grateful to Marcelo Chamecki, Chris Davis, Ralph Foster, Daniel Stern, and Margaret LeMone for insightful discussions. We acknowledge high-performance computing (HPC) support from Yellowstone (ark:/85065/d7wd3xhc) provided by NCAR's Computational and Information Systems Laboratory, sponsored by NSF; HPC support was also provided by the Texas Advanced Computing Center (TACC) at The University of Texas at Austin (http://www.tacc.utexas.edu).

APPENDIX

Representing Curved Flow in a Cartesian LES

a. *Governing equations in cylindrical and Cartesian coordinates*

The incompressible Navier–Stokes equations in cylindrical coordinates are

$$\frac{\partial u_r}{\partial t} + u_r\frac{\partial u_r}{\partial r} + \frac{v_\phi}{r}\frac{\partial u_r}{\partial \phi} + w\frac{\partial u_r}{\partial z} - \frac{v_\phi^2}{r} = -\frac{1}{\rho}\frac{\partial p}{\partial r} + \nu\left(\nabla^2 u_r - \frac{u_r}{r^2} - \frac{2}{r^2}\frac{\partial v_\phi}{\partial \phi}\right), \tag{A1a}$$

$$\frac{\partial v_\phi}{\partial t} + u_r\frac{\partial v_\phi}{\partial r} + \frac{v_\phi}{r}\frac{\partial v_\phi}{\partial \phi} + w\frac{\partial v_\phi}{\partial z} + \frac{u_r v_\phi}{r} = -\frac{1}{\rho}\frac{1}{r}\frac{\partial p}{\partial \phi} + \nu\left(\nabla^2 v_\phi - \frac{v_\phi}{r^2} + \frac{2}{r^2}\frac{\partial u_r}{\partial \phi}\right), \quad \text{and} \tag{A1b}$$

$$\frac{\partial w}{\partial t} + u_r\frac{\partial w}{\partial r} + \frac{v_\phi}{r}\frac{\partial w}{\partial \phi} + w\frac{\partial w}{\partial z} = -\frac{1}{\rho}\frac{\partial p}{\partial z} + g\frac{\theta'}{\theta_0} + \nu\nabla^2 w, \tag{A1c}$$

where (u_r, v_ϕ, w) are the velocity components in the respective radial, azimuthal, and vertical (r, ϕ, z) directions; ρ, p, and ν are the density, pressure, and kinematic viscosity of air, respectively; g is the gravitational constant; θ' is the deviation from a reference potential temperature θ_0; and with the cylindrical Laplacian given by $\nabla^2 = (1/r)(\partial/\partial r)[r(\partial/\partial r)] + (1/r^2)(\partial^2/\partial\phi^2) + (\partial^2/\partial z^2)$.

The corresponding incompressible continuity equation is

$$\frac{u_r}{r} + \frac{\partial u_r}{\partial r} + \frac{1}{r}\frac{\partial v_\phi}{\partial \phi} + \frac{\partial w}{\partial z} = 0. \tag{A2}$$

Converting from cylindrical coordinates (r, ϕ, z) to Cartesian coordinates (x, y, z)—note the z direction (and thus the vertical velocity w) are the same in both coordinate systems—can be accomplished with the help of

$$(u_r, v_\phi) = (u\cos\phi + v\sin\phi, v\cos\phi - u\sin\phi) \quad \text{and} \tag{A3a}$$

$$\left(\frac{\partial}{\partial r}, \frac{1}{r}\frac{\partial}{\partial \phi}\right) = \left(\cos\phi\frac{\partial}{\partial x} + \sin\phi\frac{\partial}{\partial y}, \cos\phi\frac{\partial}{\partial y} - \sin\phi\frac{\partial}{\partial x}\right), \tag{A3b}$$

where (u, v) are the Cartesian velocity components in the (x, y) directions, respectively.

Without making any approximations to (A3), the Cartesian forms of (A1) and (A2) are

$$\frac{\partial u}{\partial t} + u\frac{\partial u}{\partial x} + v\frac{\partial u}{\partial y} + w\frac{\partial u}{\partial z} = -\frac{1}{\rho}\frac{\partial p}{\partial x} + \nu\left(\frac{\partial^2 u}{\partial x^2} + \frac{\partial^2 u}{\partial y^2} + \frac{\partial^2 u}{\partial z^2}\right), \tag{A4a}$$

$$\frac{\partial v}{\partial t} + u\frac{\partial v}{\partial x} + v\frac{\partial v}{\partial y} + w\frac{\partial v}{\partial z} = -\frac{1}{\rho}\frac{\partial p}{\partial y} + \nu\left(\frac{\partial^2 v}{\partial x^2} + \frac{\partial^2 v}{\partial y^2} + \frac{\partial^2 v}{\partial z^2}\right), \tag{A4b}$$

$$\frac{\partial w}{\partial t} + u\frac{\partial w}{\partial x} + v\frac{\partial w}{\partial y} + w\frac{\partial w}{\partial z} = -\frac{1}{\rho}\frac{\partial p}{\partial z} + g\frac{\theta'}{\theta_0} + \nu\left(\frac{\partial^2 w}{\partial x^2} + \frac{\partial^2 w}{\partial y^2} + \frac{\partial^2 w}{\partial z^2}\right), \quad \text{and} \tag{A4c}$$

$$\frac{\partial u}{\partial x} + \frac{\partial v}{\partial y} + \frac{\partial w}{\partial z} = 0. \tag{A5}$$

Because no approximations were made in (A3), the effects of curvature (i.e., radius) are hidden in the advection terms on the left-hand sides of (A4a) and (A4b). NN12 (3559–3560) attempt to retain the effects of curvature explicitly in "local Cartesian" space by approximating r with a constant radius R (following Foster 2005); doing so implicitly assumes a small variation in ϕ that can be approximated by a constant ϕ_0—specifically, $\phi \approx \phi_0 = 0$. Applying this "local Cartesian" assumption to (A3) yields the following conversion formulas:

$$(u_r, v_\phi) \approx (u, v) \quad \text{and} \tag{A6a}$$

$$\left(\frac{\partial}{\partial r}, \frac{1}{r}\frac{\partial}{\partial \phi}\right) \approx \left(\frac{\partial}{\partial x}, \frac{\partial}{\partial y}\right). \tag{A6b}$$

Converting (A1) to Cartesian coordinates using (A6) instead of (A3) results in an extra $-v(v/R)$ term on the left-hand side of (A4a) and an extra $+u(v/R)$ term on the left-hand side of (A4b).[A1] Unfortunately, the "local Cartesian" assumption yields an equation set for which the linearized barotropic vorticity equation has an instability; this was known to NN12 (see their appendix A). Their workaround—replacing the (v/R) factor in the aforementioned extra terms by the horizontally averaged velocity $(\langle v \rangle/R)$—does remove the instability. Still, NN12 miss the root cause of the instability, which is that the constant angle approximation is made *before* taking the derivative.[A2] Therefore, the "local Cartesian" approximation (A6) is problematic and should be avoided; the proper equation set in Cartesian coordinates is given by (A4) and (A5). Fortunately, the effects of curved flow can be accounted for in (A4), as shown below.

[A1] By the same reasoning, an extra u/R term should appear on the left-hand side of the continuity equation [(A5)]. However, this term was not included in the continuity equation given by NN12.

[A2] As an example, recall that $d[\sin(\phi)]/d\phi = \cos(\phi)$. If the approximation $\phi \approx \phi_0 = 0$ is made *before* taking the derivative, then $d[\sin(\phi_0)]/d\phi = d[0]/d\phi = 0$. If the approximation is made *after* taking the derivative, then $d[\sin(\phi)]/d\phi = \cos(\phi) \approx \cos(\phi_0) = 1$.

b. Curved flow as an "effective" Coriolis term

The momentum equations in Cartesian coordinates for a fixed reference frame are given by (A4) above. However, for a reference frame with a rotation vector of $\mathbf{\Omega}_{\text{tot}} = (\Omega_{\text{tot},x})\mathbf{i} + (\Omega_{\text{tot},y})\mathbf{j} + (\Omega_{\text{tot},z})\mathbf{k}$, (A4) becomes (in vector form)

$$\frac{D\boldsymbol{v}}{Dt} = -\frac{1}{\rho}\nabla p - 2\mathbf{\Omega}_{\text{tot}} \times \boldsymbol{v} + g\frac{\theta'}{\theta_0}\mathbf{k} + \nu\nabla^2\boldsymbol{v}, \tag{A7}$$

where $D/Dt \equiv \partial/\partial t + u\partial/\partial x + v\partial/\partial y + w\partial/\partial z$, $\boldsymbol{v} = u\mathbf{i} + v\mathbf{j} + w\mathbf{k}$, and $\nabla^2 = \partial^2/\partial x^2 + \partial^2/\partial y^2 + \partial^2/\partial z^2$ is the Cartesian Laplacian.

One can think of a TC as a rotating disc (with a rotation vector of $\mathbf{\Omega}_{\text{TC}} = \Omega_{\text{TC}}\mathbf{k}$). Now, suppose this rotating disc is attached to planet Earth—which, at a latitude Ψ, has a rotation vector of $\mathbf{\Omega}_{\text{earth}} = [\Omega_{\text{earth}}\cos(\Psi)]\mathbf{j} + [\Omega_{\text{earth}}\sin(\Psi)]\mathbf{k}$. The total rotation vector in the reference frame at a point on the disc is thus

$$\mathbf{\Omega}_{\text{tot}} = \mathbf{\Omega}_{\text{earth}} + \mathbf{\Omega}_{\text{TC}} = (\Omega_{\text{earth}}\cos\Psi)\mathbf{j} + (\Omega_{\text{earth}}\sin\Psi + \Omega_{\text{TC}})\mathbf{k}. \tag{A8}$$

Substituting (A8) into (A7), making the tangent plane approximation for the earth's curved surface, and expanding into component form,

$$\frac{Du}{Dt} = -\frac{1}{\rho}\frac{\partial p}{\partial x} + (f + 2\Omega_{\text{TC}})v + \nu\nabla^2 u, \tag{A9a}$$

$$\frac{Dv}{Dt} = -\frac{1}{\rho}\frac{\partial p}{\partial y} - (f + 2\Omega_{\text{TC}})u + \nu\nabla^2 v, \quad \text{and} \tag{A9b}$$

$$\frac{Dw}{Dt} = -\frac{1}{\rho}\frac{\partial p}{\partial z} + g\frac{\theta'}{\theta_0} + \nu\nabla^2 w. \tag{A9c}$$

For a Cartesian LES with periodic lateral boundaries, the gradient of the nonperiodic component of the pressure (P) can be written in terms of a balanced background wind speed V_g. If the gradient of P is taken to be in the x direction, the resulting balance equation can be recovered by dropping the acceleration and viscous terms from (A9a):

$$-\frac{1}{\rho}\frac{\partial P}{\partial x} = -(f + 2\Omega_{\text{TC}})V_g. \tag{A10}$$

For a TC in steady-state balance, its rotation velocity at a radius R can be expressed as $\Omega_{\text{TC}} = V_g/R$. Substituting this and (A10) into (A9), and denoting the periodic component of the pressure field by p', the horizontal momentum equations for the LES are based on [cf. (8a)]

$$\frac{Du}{Dt} = -\frac{1}{\rho}\frac{\partial p'}{\partial x} + \left(f + 2\frac{V_g}{R}\right)(v - V_g) + \nu\nabla^2 u \quad \text{and} \tag{A11a}$$

$$\frac{Dv}{Dt} = -\frac{1}{\rho}\frac{\partial p'}{\partial y} - \left(f + 2\frac{V_g}{R}\right)u + \nu\nabla^2 v. \tag{A11b}$$

REFERENCES

Bao, J.-W., S. A. Michelson, and J. M. Wilczak, 2002: Sensitivity of numerical simulations to parameterizations of roughness for surface heat fluxes at high winds over the sea. *Mon. Wea. Rev.,* **130,** 1926–1932, doi:10.1175/1520-0493(2002)130<1926:SONSTP>2.0.CO;2.

——, S. G. Gopalakrishnan, S. A. Michelson, F. D. Marks, and M. T. Montgomery, 2012: Impact of physics representations in the HWRFX on simulated hurricane structure and pressure–wind relationships. *Mon. Wea. Rev.,* **140,** 3278–3299, doi:10.1175/MWR-D-11-00332.1.

Beare, R. J., and Coauthors, 2006: An intercomparison of large-eddy simulations of the stable boundary layer. *Bound.-Layer Meteor.,* **118,** 247–272, doi:10.1007/s10546-004-2820-6.

Black, P. G., and Coauthors, 2007: Air–sea exchange in hurricanes: Synthesis of observations from the Coupled Boundary Layer Air–Sea Transfer Experiment. *Bull. Amer. Meteor. Soc.,* **88,** 357–374, doi:10.1175/BAMS-88-3-357.

Braun, S. A., and W.-K. Tao, 2000: Sensitivity of high-resolution simulations of Hurricane Bob (1991) to planetary boundary layer parameterizations. *Mon. Wea. Rev.,* **128,** 3941–3961, doi:10.1175/1520-0493(2000)129<3941:SOHRSO>2.0.CO;2.

Bryan, G. H., 2012: Effects of surface exchange coefficients and turbulence length scales on the intensity and structure of numerically simulated hurricanes. *Mon. Wea. Rev.,* **140,** 1125–1143, doi:10.1175/MWR-D-11-00231.1.

——, and R. Rotunno, 2009: The maximum intensity of tropical cyclones in axisymmetric numerical model simulations. *Mon. Wea. Rev.,* **137,** 1770–1789, doi:10.1175/2008MWR2709.1.

——, J. C. Wyngaard, and J. M. Fritsch, 2003: Resolution requirements for the simulation of deep moist convection. *Mon. Wea. Rev.,* **131,** 2394–2416, doi:10.1175/1520-0493(2003)131<2394:RRFTSO>2.0.CO;2.

Charnock, H., 1955: Wind stress on a water surface. *Quart. J. Roy. Meteor. Soc.,* **81,** 639–640, doi:10.1002/qj.49708135027.

Donelan, M. A., B. K. Haus, N. Reul, W. J. Plant, M. Stiassnie, H. C. Graber, O. B. Brown, and E. S. Saltzman, 2004: On the limiting aerodynamic roughness of the ocean in very strong winds. *Geophys. Res. Lett.,* **31,** L18306, doi:10.1029/2004GL019460.

Eliassen, A., and M. Lystad, 1977: The Ekman layer of a circular vortex: A numerical and theoretical study. *Geophys. Norv.,* **31,** 1–16.

Emanuel, K. A., 1986: An air-sea interaction theory for tropical cyclones. Part I. *J. Atmos. Sci.,* **43,** 585–604, doi:10.1175/1520-0469(1986)043<0585:AASITF>2.0.CO;2.

——, 1995: Sensitivity of tropical cyclones to surface exchange coefficients and a revised steady-state model incorporating eye dynamics. *J. Atmos. Sci.,* **52,** 3969–3976, doi:10.1175/1520-0469(1995)052<3969:SOTCTS>2.0.CO;2.

Fang, J., and F. Zhang, 2012: Effect of beta shear on simulated tropical cyclones. *Mon. Wea. Rev.,* **140,** 3327–3346, doi:10.1175/MWR-D-10-05021.1.

Foster, R. C., 2005: Why rolls are prevalent in the hurricane boundary layer. *J. Atmos. Sci.,* **62,** 2647–2661, doi:10.1175/JAS3475.1.

French, J. R., W. M. Drennan, J. A. Zhang, and P. G. Black, 2007: Turbulent fluxes in the hurricane boundary layer. Part I: Momentum flux. *J. Atmos. Sci.,* **64,** 1089–1102, doi:10.1175/JAS3887.1.

Gao, K., and I. Ginis, 2014: On the generation of roll vortices due to the inflection point instability of the hurricane boundary layer flow. *J. Atmos. Sci.,* **71,** 4292–4307, doi:10.1175/JAS-D-13-0362.1.

Gopalakrishnan, S. G., F. Marks, J. A. Zhang, X. Zhang, J.-W. Bao, and V. Tallapragada, 2013: A study of the impacts of vertical diffusion on the structure and intensity of the tropical cyclones using the high-resolution HWRF system. *J. Atmos. Sci.,* **70,** 524–541, doi:10.1175/JAS-D-11-0340.1.

Green, B. W., and F. Zhang, 2013: Impacts of air–sea flux parameterizations on the intensity and structure of tropical cyclones. *Mon. Wea. Rev.,* **141,** 2308–2324, doi:10.1175/MWR-D-12-00274.1.

——, and ——, 2014: Sensitivity of tropical cyclone simulations to parametric uncertainties in air–sea fluxes and implications for parameter estimation. *Mon. Wea. Rev.,* **142,** 2290–2308, doi:10.1175/MWR-D-13-00208.1.

——, and ——, 2015: Numerical simulations of Hurricane Katrina (2005) in the turbulent gray zone. *J. Adv. Model. Earth Syst.,* 07, doi:10.1002/2014MS000399.

——, ——, and P. Markowski, 2011: Multiscale processes leading to supercells in the landfalling outer rainbands of Hurricane Katrina (2005). *Wea. Forecasting,* **26,** 828–847, doi:10.1175/WAF-D-10-05049.1.

Holton, J. R., 2004: *An Introduction to Dynamic Meteorology.* Academic Press, 535 pp.

Hong, S.-Y., Y. Noh, and J. Dudhia, 2006: A new vertical diffusion package with an explicit treatment of entrainment processes. *Mon. Wea. Rev.,* **134,** 2318–2341, doi:10.1175/MWR3199.1.

Kepert, J. D., 2001: The dynamics of boundary layer jets within the tropical cyclone core. Part I: Linear theory. *J. Atmos. Sci.,* **58,** 2469–2484, doi:10.1175/1520-0469(2001)058<2469:TDOBLJ>2.0.CO;2.

——, 2010: Slab- and height-resolving models of the tropical cyclone boundary layer. Part I: Comparing the simulations. *Quart. J. Roy. Meteor. Soc.,* **136,** 1689–1699, doi:10.1002/qj.667.

——, 2012: Choosing a boundary layer parameterization for tropical cyclone modeling. *Mon. Wea. Rev.,* **140,** 1427–1445, doi:10.1175/MWR-D-11-00217.1.

——, 2013: How does the boundary layer contribute to eyewall replacement cycles in axisymmetric tropical cyclones? *J. Atmos. Sci.,* **70,** 2808–2830, doi:10.1175/JAS-D-13-046.1.

——, and Y. Wang, 2001: The dynamics of boundary layer jets within the tropical cyclone core. Part II: Nonlinear enhancement. *J. Atmos. Sci.,* **58,** 2485–2501, doi:10.1175/1520-0469(2001)058<2485:TDOBLJ>2.0.CO;2.

Klemp, J., and D. Durran, 1983: An upper boundary condition permitting internal gravity wave radiation in numerical mesoscale models. *Mon. Wea. Rev.,* **111,** 430–444, doi:10.1175/1520-0493(1983)111<0430:AUBCPI>2.0.CO;2.

Kosović, B., and J. A. Curry, 2000: A large eddy simulation study of a quasi-steady, stably stratified atmospheric boundary layer. *J. Atmos. Sci.,* **57,** 1052–1068, doi:10.1175/1520-0469(2000)057<1052:ALESSO>2.0.CO;2.

Moeng, C.-H., 1984: A large-eddy-simulation model for the study of planetary boundary-layer turbulence. *J. Atmos. Sci.,* **41,** 2052–2062, doi:10.1175/1520-0469(1984)041<2052:ALESMF>2.0.CO;2.

——, and P. P. Sullivan, 1994: A comparison of shear- and buoyancy-drive planetary boundary layer flows. *J. Atmos. Sci.,* **51,** 999–1022, doi:10.1175/1520-0469(1994)051<0999:ACOSAB>2.0.CO;2.

Montgomery, M. T., R. K. Smith, and S. V. Nguyen, 2010: Sensitivity of tropical-cyclone models to the surface drag coefficient. *Quart. J. Roy. Meteor. Soc.,* **136,** 1945–1953, doi:10.1002/qj.702.

Morrison, I., S. Businger, F. Marks, P. Dodge, and J. A. Businger, 2005: An observational case for the prevalence of roll vortices in the hurricane boundary layer. *J. Atmos. Sci.,* **62,** 2662–2673, doi:10.1175/JAS3508.1.

Nakanishi, M., 2000: Large-eddy simulation of radiation fog. *Bound.-Layer Meteor.,* **94,** 461–493, doi:10.1023/A:1002490423389.

——, and H. Niino, 2012: Large-eddy simulation of roll vortices in a hurricane boundary layer. *J. Atmos. Sci.,* **69,** 3558–3575, doi:10.1175/JAS-D-11-0237.1.

Nolan, D. S., J. A. Zhang, and D. P. Stern, 2009a: Evaluation of planetary boundary layer parameterizations in tropical cyclones by comparison of in situ observations and high-resolution simulations of Hurricane Isabel (2003). Part I: Initialization, maximum winds, and the outer-core boundary layer. *Mon. Wea. Rev.,* **137,** 3651–3674, doi:10.1175/2009MWR2785.1.

——, D. P. Stern, and J. A. Zhang, 2009b: Evaluation of planetary boundary layer parameterizations in tropical cyclones by comparison of in situ observations and high-resolution simulations of Hurricane Isabel (2003). Part II: Inner-core boundary layer and eyewall structure. *Mon. Wea. Rev.,* **137,** 3675–3698, doi:10.1175/2009MWR2786.1.

Ooyama, K., 1969: Numerical simulation of the life cycle of tropical cyclones. *J. Atmos. Sci.,* **68,** 1586–1606.

Powell, M. D., E. W. Uhlhorn, and J. D. Kepert, 2009: Estimating maximum surface winds from hurricane reconnaissance measurements. *Wea. Forecasting,* **24,** 868–883, doi:10.1175/2008WAF2007087.1.

Rosenthal, S. L., 1971: The response of a tropical cyclone model to variations in boundary layer parameters, initial conditions, lateral boundary conditions, and domain size. *Mon. Wea. Rev.,* **99,** 767–777, doi:10.1175/1520-0493(1971)099<0767:TROATC>2.3.CO;2.

Rotunno, R., and J. B. Klemp, 1982: The influence of the shear-induced pressure gradient on thunderstorm motion. *Mon. Wea. Rev.,* **110,** 136–151, doi:10.1175/1520-0493(1982)110<0136:TIOTSI>2.0.CO;2.

——, and G. H. Bryan, 2012: Effects of parameterized diffusion on simulated hurricanes. *J. Atmos. Sci.,* **69,** 2284–2299, doi:10.1175/JAS-D-11-0204.1.

——, Y. Chen, W. Wang, C. Davis, J. Dudhia, and G. J. Holland, 2009: Large-eddy simulation of an idealized tropical cyclones. *Bull. Amer. Meteor. Soc.,* **90,** 1783–1788, doi:10.1175/2009BAMS2884.1.

Shpund, J., M. Pinsky, and A. Khain, 2011: Microphysical structure of the marine boundary layer under strong wind and spray formation as seen from simulations using a 2D explicit microphysical model. Part I: The impact of large eddies. *J. Atmos. Sci.,* **68,** 2366–2384, doi:10.1175/2011JAS3652.1.

——, J. A. Zhang, M. Pinsky, and A. Khain, 2012: Microphysical structure of the marine boundary layer under strong wind and spray formation as seen from simulations using a 2D explicit microphysical model. Part II: The role of sea spray. *J. Atmos. Sci.,* **69,** 3501–3514, doi:10.1175/JAS-D-11-0281.1.

——, ——, ——, and ——, 2014: Microphysical structure of the marine boundary layer under strong wind and sea spray formation as seen from a 2D explicit microphysical model. Part III: Parameterization of height-dependent droplet size distribution. *J. Atmos. Sci.,* **71,** 1914–1934, doi:10.1175/JAS-D-12-0201.1.

Smith, R. K., M. T. Montgomery, and N. Van Sang, 2009: Tropical cyclone spin-up revisited. *Quart. J. Roy. Meteor. Soc.,* **135,** 1321–1335, doi:10.1002/qj.428.

——, ——, and G. L. Thomsen, 2014: Sensitivity of tropical-cyclone models to the surface drag coefficient in different boundary-layer schemes. *Quart. J. Roy. Meteor. Soc.,* **140,** 792–804, doi:10.1002/qj.2057.

Sullivan, P. P., and E. G. Patton, 2011: The effect of mesh resolution on convective boundary layer statistics and structures generated by large-eddy simulation. *J. Atmos. Sci.,* **68,** 2395–2415, doi:10.1175/JAS-D-10-05010.1.

——, J. C. McWilliams, and C.-H. Moeng, 1994: A subgrid-scale model for large-eddy simulation of planetary boundary-layer flows. *Bound.-Layer Meteor.,* **71,** 247–276, doi:10.1007/BF00713741.

——, ——, and ——, 1996: A grid nesting method for large-eddy simulation of planetary boundary-layer flows. *Bound.-Layer Meteor.,* **80,** 167–202, doi:10.1007/BF00119016.

——, C.-H. Moeng, B. Stevens, D. Lenschow, and S. D. Mayor, 1998: Structure of the entrainment zone capping the convective atmospheric boundary layer. *J. Atmos. Sci.,* **55,** 3042–3064, doi:10.1175/1520-0469(1998)055<3042:SOTEZC>2.0.CO;2.

Wang, X., Y. Ma, and N. E. Davidson, 2013: Secondary eyewall formation and eyewall replacement cycles in a simulated hurricane: Effect of the net radial force in the hurricane boundary layer. *J. Atmos. Sci.,* **70,** 1317–1341, doi:10.1175/JAS-D-12-017.1.

Wurman, J., and J. Winslow, 1998: Intense sub-kilometer-scale boundary layer rolls observed in Hurricane Fran. *Science,* **280,** 555–557, doi:10.1126/science.280.5363.555.

Zhang, J. A., and W. M. Drennan, 2012: An observational study of vertical eddy diffusivity in the hurricane boundary layer. *J. Atmos. Sci.,* **69,** 3223–3236, doi:10.1175/JAS-D-11-0348.1.

——, P. G. Black, J. R. French, and W. M. Drennan, 2008a: First direct measurements of enthalpy flux in the hurricane boundary layer: The CBLAST results. *Geophys. Res. Lett.,* **35,** L14813, doi:10.1029/2008GL034374.

——, K. B. Katsaros, P. G. Black, S. Lehner, J. R. French, and W. M. Drennan, 2008b: Effects of roll vortices on turbulent fluxes in the hurricane boundary layer. *Bound.-Layer Meteor.,* **128,** 173–189, doi:10.1007/s10546-008-9281-2.

——, F. D. Marks, M. T. Montgomery, and S. Lorsolo, 2011a: An estimation of turbulent characteristics in the low-level region of intense hurricanes Allen (1980) and Hugo (1989). *Mon. Wea. Rev.,* **139,** 1447–1462, doi:10.1175/2010MWR3435.1.

——, R. F. Rogers, D. S. Nolan, and F. D. Marks, 2011b: On the characteristic height scales of the hurricane boundary layer. *Mon. Wea. Rev.,* **139,** 2523–2535, doi:10.1175/MWR-D-10-05017.1.

Zhu, P., 2008: Simulation and parameterization of the turbulent transport in the hurricane boundary layer by large eddies. *J. Geophys. Res.,* **113,** D17104, doi:10.1029/2007JD009643.